Structural Evolution of Layered Hybrid Lead Iodide Perovskites in Colloidal Dispersions

Clayton J. Dahlman,[†] Naveen R. Venkatesan,[†] Patrick T. Corona,[‡] Rhys M. Kennard,[†] Lingling Mao,[†] Noah C. Smith,[‡] Jiamin Zhang,[‡] Ram Seshadri,[†,+] Matthew E. Helgeson,[‡] Michael L. Chabinyc[†,*]

[†] Materials Department, University of California, Santa Barbara, CA 93106, United States

[‡] Department of Chemical Engineering, University of California, Santa Barbara, CA 93106, United States

[+]Department of Chemistry and Biochemistry, University of California, Santa Barbara, CA 93106, United States

*Corresponding Author: mchabinyc@engineering.ucsb.edu

Abstract

Controlling the structure of layered hybrid metal halide perovskites, such as the Ruddlesden-Popper (R-P) phases, is challenging because of their tendency to form mixtures of varying composition. Colloidal growth techniques, such as antisolvent precipitation, forms colloidal dispersions with properties that match bulk layered R-P phases, but controlling the composition of these particles remains challenging. Here, we explore the microstructure of particles of R-P phases of methylammonium lead iodide prepared by antisolvent precipitation from ternary mixtures of alkylammonium cations, where one cation can form perovskite phases ($CH_3NH_3^+$) and the other two promote layered structures as spacers (*e.g.* $C_4H_9NH_3^+$ and $C_{12}H_{25}NH_3^+$). We determine that alkylammonium spacers pack with constant methylene density in the R-P interlayer, and exclude interlayer solvent in dispersed colloids, regardless of length or branching. Using this result, we illustrate how the competition between cations that act as spacers between layers, or as grain-terminating ligands, determines the colloidal microstructure of layered R-P crystallites in solution. Optical measurements reveal that quantum well dimensions can be tuned by engineering the ternary cation composition. Transmission synchrotron wide-angle X-ray scattering and small angle neutron scattering reveal changes in the structure of colloids in solvent and after deposition into thin films. In particular, we find that spacers can alloy between R-P layers if they share common steric arrangements, but tend to segregate into polydisperse R-P phases if they do not mix. This study provides a framework to compare the microstructure of colloidal layered perovskites and suggests clear avenues to control phase and colloidal morphology.

Keywords

lead halide perovskite, colloid, 2D, Ruddlesden-Popper, nanocrystal, neutron scattering, X-ray diffraction

TOC:

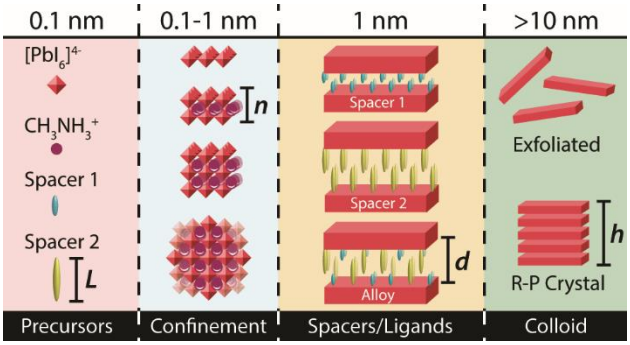

Hybrid organic inorganic perovskites (HOIPs) have remarkable optical and electronic properties allowing growth of thin film optoelectronic devices at low-temperature.[1–5] Ruddlesden-Popper (R-P) phases of HOIP materials provide a route to modify the optoelectronic properties with the benefit of improved stability in the ambient.[6,7] 2D perovskites have a well-defined thickness between lead halide layers, affected by both the number of lead halide octahedra in each layer (*e.g.* the '*n*' value for the Ruddlesden-Popper phases with composition $R_2A_{n-1}Pb_nX_{3n+1}$) and the insulating spacer cations (*R*), such as butylammonium (C4) or phenethylammonium (PEA).[6,8–14]

The structure of Ruddlesden-Popper phases of hybrid organic inorganic perovskites presents an interesting challenge for controlling the functionalization of their surfaces. Here we examine how interactions between alkylammonium compounds influence the growth of R-P phases of methylammonium lead iodide ($MAPbI_3$). The spacer cations, *R*, effectively cap the surface of the inorganic layers while being a constituent of the material. This feature contrasts the function of organic groups in inorganic nanoparticles where ligands are only attached to the outer surface of the material and cannot be incorporated directly into the structure. By studying the growth of colloidal crystals with different mixtures of alkylammonium groups, we find that these groups can either alloy along the R-P lead halide surface or segregate into distinct domains, with systematic effects on the colloidal stability and layering structure (*n*-value).

The development of 2D layered perovskites for thin film applications has been hampered by challenges to control *n*-value phase purity and grain microstructure. Phase-pure R-P single crystals have been grown with controlled layering up to $n = 7$,[15–17] but control over phase purity for thin films of R-Ps is difficult for $n > 2$.[18–24] One avenue to tailor the grain structure and phase of 2D perovskites is through colloidal synthesis. Colloidal perovskite nanocrystals can have improved luminescence quantum yield compared to bulk counterparts,[25–30] and have been used to make high-performing photovoltaic and light-emitting devices.[31–33] Molecular design rules for surface ligands that can stabilize the surfaces of R-P phases, while not readily incorporating into the lattice, would lead to better control of the growth of these materials.

The soft ionic structure of hybrid perovskites allows for a great versatility in colloidal synthesis techniques. Two methods in particular, hot-injection of precursors in a surfactant-rich solution and ligand assisted re-precipitation of precursors in an antisolvent, are commonly used to form perovskite nanocrystals with controlled size, shape and phase. Precise size and shape control of monodisperse larger particles (> 5 nm) has been achieved with both hot-injection and re-precipitation techniques, but colloidal perovskites tend to aggregate, degrade or segregate when one of their dimensions approaches the quantum confinement threshold (< 5 nm).[34–37] The ligand, synthesis temperature, perovskite composition and concentration all have significant impacts on the lateral dimension, thickness and polydispersity of 2D perovskite colloids

prepared by re-precipitation.[25,34,35,37–47] Control over thickness is particularly difficult for particles larger than two lead halide octahedra thick (*i.e.* $n > 2$). Typically, emission from mixtures of different *n*-values is observed, and the colloids phase segregate over time.[41,42,48] The instability of 2D colloidal perovskites, both to aging and photodegradation, has been attributed to the reactivity of the colloid surface and rapid exchange of ions within dispersions and films.[49,50] The dynamic interaction between surfactant species and lead halide sheets, both within 2D perovskite grains and at the solvent interface, presents a unique challenge to control the microstructure of colloidal perovskites.

The microstructure of colloidal perovskites is defined by interfaces between perovskite regions and insulating spacers, ligands or solvent. The 'ligands' that are typically used to stabilize perovskite colloids are protonated amines (either added directly as ammonium salts or through protonation from carboxylic acids in the dispersion) and may form layered R-P phases themselves, as spacers. This observation is frequently described as 'agglomeration' and 'superlattice' formation.[36,43,47,51–53] Determining if stacks of smaller 2D crystallites lead to an ordered structure can be challenging and is akin to the study of grain boundaries in solids. An additional complexity is whether very small nanoparticles of 3D-phases have comparable optical properties due to confinement, particularly with respect to higher *n* R-P phases. For example, the unit cell of an $n = 7$ R-P phase is nearly 5 nm along the layering dimension,[15,16] comparable to the upper size limit for quantum confinement in cubic or spherical perovskite nanocrystals.[25,30,54–57] Thus, a careful accounting of interactions between surfactant species that can stabilize perovskite interfaces is necessary to control colloidal perovskite growth.

We examine here the growth of colloids of R-P phases of $MAPbI_3$ using varying alkylammonium cations to determine how cation structure contributes to colloidal 2D perovskite formation. By comparing the structure and optoelectronic properties of 2D perovskite colloids both in dispersions (at dilute and concentrated limits) and as deposited films, we can understand the factors in structural evolution from isolated crystallites to a dense film. Use of a controlled set of ligand and spacer molecules, with varying compositions, reveals the significance of aggregation in solution to the phase and microstructure of colloidal 2D perovskites. The combination of X-ray and neutron scattering in solution is critical to understand the evolution of the phases.

Results and Discussion

A description of the structure of 2D perovskite colloids is complicated by the different interfaces present between lead halide octahedra. We begin by describing a framework to define the multiscale structure of colloidal 2D perovskites in dispersions with mixed cations. Next, we explore the limits of colloidal 2D perovskite formation with different spacer cations. Finally, we investigate how competition between mixtures of different spacer cations directs the phase and microstructure of colloidal R-P phases.

Defining the microstructure of 2D perovskite colloids. $MAPbI_3$ quantum-confined nanoparticles and 2D layered (*i.e.* R-P or Dion-Jacobson (D-J)) crystalline particles (at all size scales) are difficult to distinguish by their optical properties. The Bohr radius of $MAPbI_3$ is about 2 nm, and similar to $MAPbBr_3$.[58] Size-dependent shifts in optical emission are observed in spherical $MAPbBr_3$ nanocrystals at sizes of 10 nm in diameter ($\Delta E \sim 40$ meV).[59] R-P phases with $n = 7$ derived from $MAPbI_3$, with confined layers of about 5 nm in thickness, also show a blue-shifted band-gap ($\Delta E \sim 150$ meV)[15] The optical absorption and emission of R-P and D-J phases are also sensitive to the dielectric contrast between the inorganic and organic layers,[60–65] such that an image charge effect triples the exciton binding energy in $n = 1$ R-Ps.[66] Determining whether nanoparticles of layered R-P and D-J phases form is especially challenging because photoluminescence (PL) and absorbance measurements are more sensitive to the confined dimension of layers (n value) than the size and shape of assembled crystallites, as shown in **Figure 1b**. In light of these challenges, SEM, TEM and AFM are often relied upon to characterize the microstructure of 2D perovskite colloids, but these methods require transfer of diluted colloidal particles to substrates.

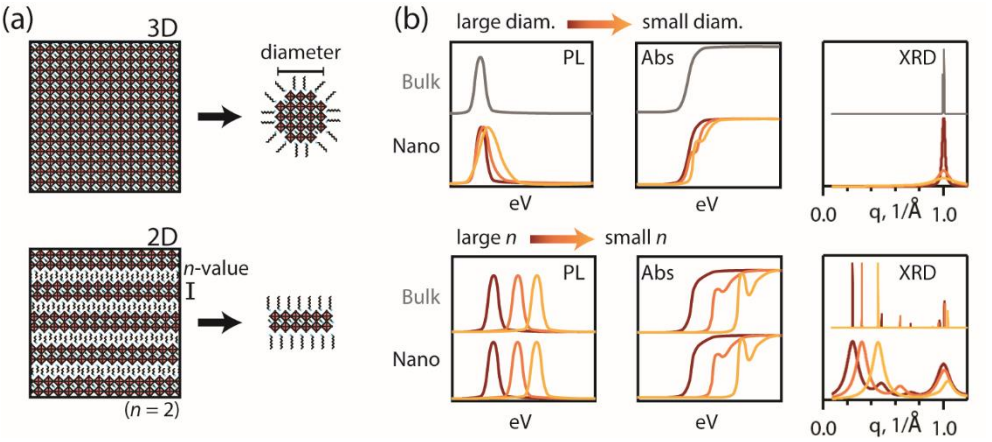

Figure 1. a) A schematic comparing the bulk and nanoscale structure of 3D and 2D perovskites. b) Expected PL and absorbance spectra for each case are shown as function of nanoscale confinement, along with expected XRD patterns.

The microstructure of colloidal 2D perovskites is determined by how ammonium cations incorporate in the bulk and on the surface of lead iodide octahedra. Unlike semiconductor nanocrystals such as metal oxides or chalcogenides, the ionic NH_3^+-$[PbI_x]^-$ bonds within layers of R-P-phases are indistinguishable from the bonds at the surface.[67] Cations bound at the grain surface interact with the solvent and behave similarly to ligands on nanoparticles, while cations bound between lead halide sheets are the spacers in the R-P structures (**Figure 2**). Mixtures of different insulating ligands, containing both shorter alkylammonium species, such as *n*-butylammonium (C4), and longer species, such as *n*-octylammonium (C8), have produced colloidal dispersions with greater stability and phase purity than single-component compositions.[38,68] These observations suggest a distinction between 'spacers' and 'ligands' (**Figure 2**), which may be exploited to control the microstructure of colloidal 2D perovskites. Spacers separate lead iodide octahedra layers and determine the *n* value, while ligands passivate the surface and determine the grain 'height' and 'width'.

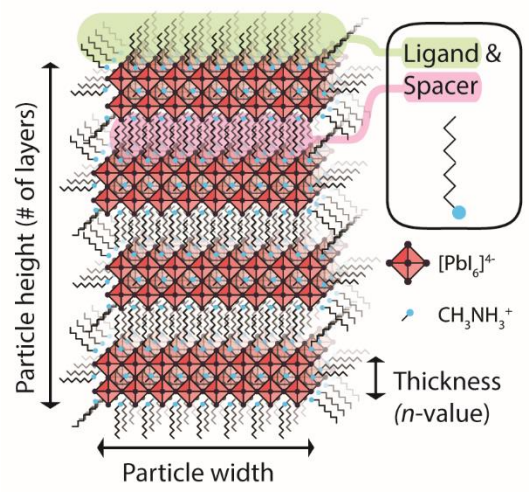

Figure 2. A schematic illustrating the different length scales of structure for colloidal perovskite nanoplatelets in dispersion, indicating the particle 'height', 'width' and layer 'thickness'. The particle shown consists of a 4-layer n = 2 Ruddlesden-Popper phase with octylammonium spacers, and is terminated by ligands of the same octylammonium spacers.

A variety of molecules have been explored to separate 2D perovskite layers. The spacer molecule, such as butylammonium (C4) in $C4_2MA_{n-1}Pb_nI_{3n+1}$ R-P phases,[8] needs a positively charged group (typically ammonium) to bind with negative sites along the octahedral [PbI_6] lattice, a functional group to separate the 2D layers, and a size that fits within the spatial constraint of the lattice. Notably, these conditions are not met by several surfactant additives used to stabilize perovskite nanocrystal dispersions with larger dimensions. Additives such as pyridine,[43] zwitterionic ligands,[69] acetates[50] and trioctylphosphine[27,55] can stabilize dispersions of $MAPbX_3$ and $CsPbX_3$ nanocrystals,[49] but cannot charge-compensate the perovskite sub-phase in an R-P or D-J crystal. Linear primary alkylammonium species have been studied in great detail as spacers, ranging from ethylammonium (C2) to octadecylammonium (C18).[13,70–75] Longer spacers are often explored because they can improve the stability of colloidal dispersions in non-polar solvents,[76] but the interaction between spacer and ligand behavior of longer species in 2D perovskite colloids is unclear.

Designing an appropriate surfactant mixture to stabilize phase-pure colloids of 2D perovskites requires a careful assessment of microstructure in dispersions and deposited films. First, we describe how the length and breadth of alkylammonium spacers changes the layering structure of colloidal R-P phases. Next, we explore how mixtures of spacers with different shapes and sizes can interact to control colloidal perovskite phase (*i.e.* n-value), interlayer separation and particle dimensions.

Forming 2D layered perovskites with different spacers. The surface functionalization of bulk 2D perovskites, or colloidal perovskites, is affected by the chemical structure of interlayer or surface-capping ammonium species. To examine this composition dependence, 2D perovskite colloids were synthesized by antisolvent precipitation of a salt solution ($MAPbI_3$ and spacer precursors) following established techniques.[68] The concentration of the precursor solution, and quantity of precursor added to the antisolvent, yielded colloidal dispersions about 25× higher in concentration (2.5 mmol Pb/L) than in previous reports[68] to simulate the higher particle loadings appropriate for device coatings. Particle concentration can impact both 2D perovskite thickness (the *n* value) and grain size,[39] but it is unclear if these effects manifest during the initial precipitation from precursors or upon aging of the dispersed colloid. The effects of dilution were tested when applicable (*vide infra*).

Linear alkylammonium cations. We first sought to determine whether the interlayer separation of drop-cast 2D perovskite colloids and single crystals of R-P phases are identical for the same linear alkylammonium cation. Previous studies suggested that solvent can incorporate between layers during R-P growth,[36] so it is important to determine if entrapped solvent changes the interlayer structure of dispersed colloids. As an example, colloids prepared through antisolvent precipitation of $\langle n \rangle = 2$ $R_2MAPb_2I_7$ precursors were synthesized with linear alkylammonium spacers (*R*) of different lengths. The XRD of drop-cast films of colloidal dispersions prepared by antisolvent re-precipitation are given in **Figure 3a**. Diffraction from $n = 2$ is observed by characteristic reflections from the layer-stacking (0*k*0) plane along with the presence of $n = 1$ phases for the longest alkylammonium cations. Crystallites of the drop-cast films are highly textured, showing only (0*k*0) reflections oriented normal to the substrate.[48] The (0*k*0) reflections provide the unit cell *b* parameter (assuming an analogous unit cell for the different spacers), which depends on both the *n*-value (*i.e.* the thickness of the lead iodide sheets) and the separation between lead iodide layers (**Figure 3c**).

The distance between adjacent lead halide surfaces, which contains the organic spacer sub-phase, can be estimated from the *d*-spacing and approximate PbI_6 octahedral dimensions (**Figure S2**). The interlayer separation between lead iodide sheets of the drop-cast $n = 2$ phases follows a linear relationship with the number of carbon atoms in the spacer molecule (**Figure 3b**, red circles). This trend matches expectations from room-temperature single-crystal diffraction of $n = 1$ R-P phases from the literature.[70,72–75] The slope of this scaling, 1.36 Å per additional methylene unit, is slightly greater than the incremental length, 1.265 Å, of an additional methylene unit of an all-*trans* alkane molecule[77] **Figure 3b**. To rationalize the scaling, either the methylene units are arranged in an all-*trans* conformation with a tilt angle θ of ≈55° to prevent interdigitation,[74] or they are interdigitated in a nearly all-*trans* conformation with a defective region near

the ammonium group.[72,73,75] Regardless of the conformation of the alkyl groups, the lead iodide sheets in the colloids are layered like single-crystal R-P phases for a range of spacer molecules.

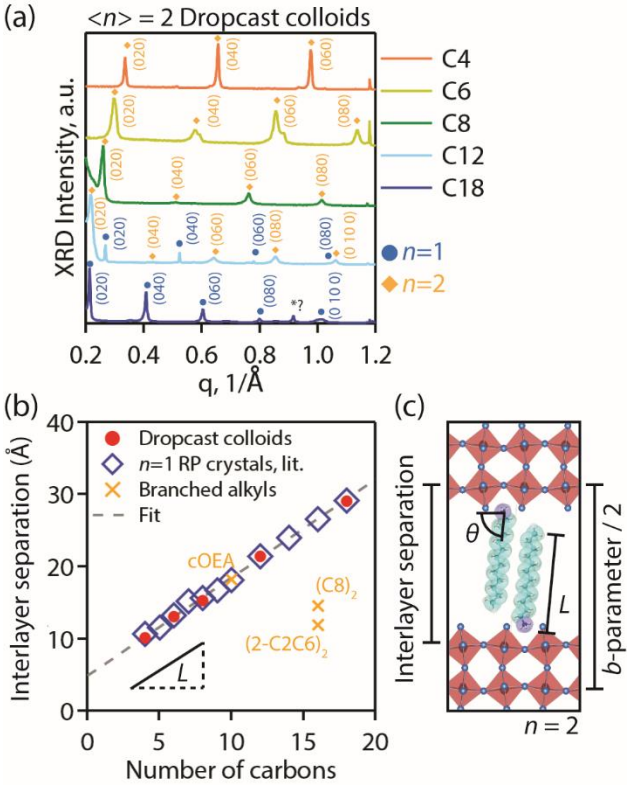

Figure 3. Properties of colloidal perovskites prepared with an average precursor stoichiometry of <*n*> = 2 for alkylammonium spacers. a) XRD of dropcast colloidal perovskites prepared with an <*n*> = 2 precursor stoichiometry for linear alkylammonium spacers. The red circles indicate *n* = 1 (0*k*0) peaks and the blue diamonds indicate *n*=2 (0*k*0) peaks. b) Estimated interlayer separations calculated from unit cell parameters obtained by XRD. The red circles show measured values obtained from the (0*k*0) peaks in a), and the blue diamonds indicate values estimated from published unit cell parameters of single crystalline *n* = 1 R-P phases at room temperature.[72,73,75] Orange X markers indicate values for branched alkylammonium spacers. The dashed grey line indicates a line of best fit through the red circles and blue diamonds. The slope indicated by *L* refers to the scaling expected for interdigitated all-*trans* linear alkylammonium molecules oriented normal ($\theta = 90°$) to lead iodide octahedral layers. c) A schematic of *n* = 2 $C12_2MAPb_2I_7$ illustrating interlayer separation and *b* parameter dimensions, as well as the spacer end-to-end length, *L*, and tilt angle from the perovskite surface, θ.

PL reveals that other *n*-value phases are present in colloidal dispersions of R-Ps with a nominal composition of $\langle n \rangle = 2$. Colloids prepared with shorter spacers (C4-C8) show photoluminescence from $n = 2$, 3 and higher-*n* phases (**Figure S3**), despite XRD diffraction patterns of drop-cast films indicating phase pure $n = 2$ structures (**Figure 3a**). This discrepancy may relate to either the sensitivities of each technique to different phases,[18,20] or to different structures that form in drop-cast vs. dispersed 2D perovskites. Even if $n = 2$ R-P phases form the majority of the colloidal material for C4, C6 and C8 spacers, the presence of lower bandgap phases can dominate optical and electronic properties in devices.[18,20,78] Phase segregation is more pronounced for colloids prepared from the longest spacers (C12, C18), with polyphasic PL spectra (**Figure S3**) and XRD patterns that can be indexed to $n = 1$ R-P phases (**Figure 3a**), instead of the nominal $n = 2$ phase. The causes of phase segregation in 2D perovskites formed by spin-coating, antisolvent precipitation and other methods are actively debated. Phase segregation may originate from differences in the formation energy of 2D perovskites with different *n*-values,[15] the kinetics of nucleation and growth of 2D perovskite phases,[23,40] or even the energetics of spacer-spacer and spacer-solvent interactions during growth.[76,79,80]

Cyclic and branched alkylammonium cations. An alternative spacer, *n*-cyclooctylethylammonium (cOEA) was explored to change the steric repulsions between spacers and to modify the intermolecular interactions. Branched or cyclic alkyl species have lower melting points and mixing enthalpies than linear alkyl species with the same number of methylene units.[81] Thus, the energetics of colloidal 2D perovskite growth may differ from synthesis with linear alkylammonium precursors. To our knowledge, cOEA has not been explored for the synthesis of crystalline 2D perovskite phases or colloidal perovskite nanocrystals, although cyclohexylmethylammonium spacers have been used to prepare spin-coated R-P films.[82]

In its unsubstituted form, cOEA has a number of low energy (within < 4 kcal/mol) conformations that can interconvert that should alter packing in between the inorganic layers.[83] If we consider the lowest energy boat-chair conformation, the cyclooctyl ring is ~5.2 Å across from hydrogen to hydrogen at its widest point, which is larger than the size of the comparable dimension in the benzene ring of phenyl ethylamine (~4.2 Å). The addition of the van der Waals (vdW) radii increase the dimension of the cyclooctyl ring to ~7.6 Å which is slightly larger than the diagonal Pb-Pb distance in the inorganic layer (6.3 Å). The cOEA molecule will therefore be more spatially constrained than the linear alkyl amines. Despite the frustrated areal packing expected for cOEA on the perovskite surface, it can still form layered 2D perovskite phases of $n = 1$ R-Ps with characteristic emission and diffraction signatures (**Figure 4**).

We found that layered perovskites formed from cOEA and linear spacers have interlayer separations determined by atomic density, rather than the length or branching of alkylammonium molecules. All of the linear alkylammonium cations (*e.g.* C4, C8, C12, C18) have identical areal footprints (~5.4 Å H-H distance with vdW radii) when present in all-*trans* configurations. This is much smaller than the diagonal I-I distance across the octahedral site (6.3 Å). cOEA has a significantly larger areal foot-print than the linear alkylammonium species that seems to be slightly larger than the octahedral site. Nonetheless, colloidal 2D perovskites prepared with n = 1 compositions of C4, C12 and cOEA spacers yield diffraction patterns and optical properties consistent with n = 1 lead iodide R-P crystals (**Figure 4**). XRD of dropcast n = 1 C12 and cOEA colloids show characteristic n = 1 R-P (0k0) reflections, and PL and absorbance of colloidal dispersions show optical emission and excitonic absorption around the expected 520 nm peak for n = 1 R-P phases.[8] The interlayer distance estimated for cOEA from XRD matches the spacing expected for decylammonium iodide (C10) of 18.2 Å (**Figure 3b**). The end-to-end length of cOEA (12.0 Å H-H distance with vdW radii) is shorter than decylammonium (~16.9 Å H-H distance with vdW radii). Thus, the interlayer spacing for alkylammonium spacers is dictated by the atomic density (0.037 C atoms/Å^3) within the organic sub-phase, rather than the extended length of the spacer molecules. We note that the interlayer density of carbon atoms within R-P phases is nearly identical to that of amorphous polyetheylene (0.038 C atoms/Å^3). This behavior is different from the packing of intercalated surfactants in the galleries of layered clays and double hydroxides, which undergo significant changes in interlayer packing density with composition or temperature.[84] The constant methylene packing density in the R-P interlayer may guide the selection of spacer cations, and provides a useful characterization tool as described later in the manuscript.

In contrast to the linear and cyclic cations we studied, branched ammonium species strongly perturb the ability to form R-P phases. **Figure 4a** illustrates the areal footprints of two binary ammonium species: dioctylammonium ($(C8)_2$) and bis-2-ethylhexylammonium ($(2\text{-}C2C6)_2$). Both of these molecules have 16 methylene units, but the branching should impede close packing of these molecules. Neither of these branched spacers with n = 1 stoichiometry formed colloidal particles that could be precipitated through centrifugation after antisolvent precipitation. XRD and PL of the unwashed product of antisolvent precipitation from these spacers is shown in **Figure 4**. Although an extremely faint PL emission around 520 nm was observed for both $(C8)_2$ and $(2\text{-}C2C6)_2$ colloidal dispersions (magnified by 50× to highlight the peak in **Figure S4**), absorbance measurements reveal that any n = 1 phase is a small minority of the total material. A much stronger absorbance feature around 370 nm for each of these larger branched spacers is consistent with $[PbI_3]^-$ complexes observed in DMF solutions, suggesting they form solvated lead iodide complexes instead of 2D perovskite phases.[85] These results are consistent with earlier observations that

binary and ternary octylammonium spacers do not form 2D $CsPbBr_3$ R-P colloids by antisolvent precipitation, even though primary *n*-octylammonium produces a range of low *n*-value phases.[41]

Drop-cast films from $(C8)_2$ and $(2\text{-}C2C6)_2$ spacers show repeating reflections by XRD (**Figure 4b**). Neither film can be indexed to solvate phases with comparable structures to $(MA)(DMF)(PbI_3)$,[20] nor do these phases show optical PL or absorption consistent with 2D R-Ps. If these spacers did form R-P layered structures based on the dominant *d*-spacing in the XRD, the methylene density within the interlayer would be much greater ($\approx$ 0.1 C atoms/Å^3) than for an analogous 16 carbon alkylammonium spacer (**Figure 3b**). The large atomic densities required to pack these spacers along a lead iodide perovskite surface suggests that an alternative structure is formed that lacks continuous bonding between PbI_6 octahedra.

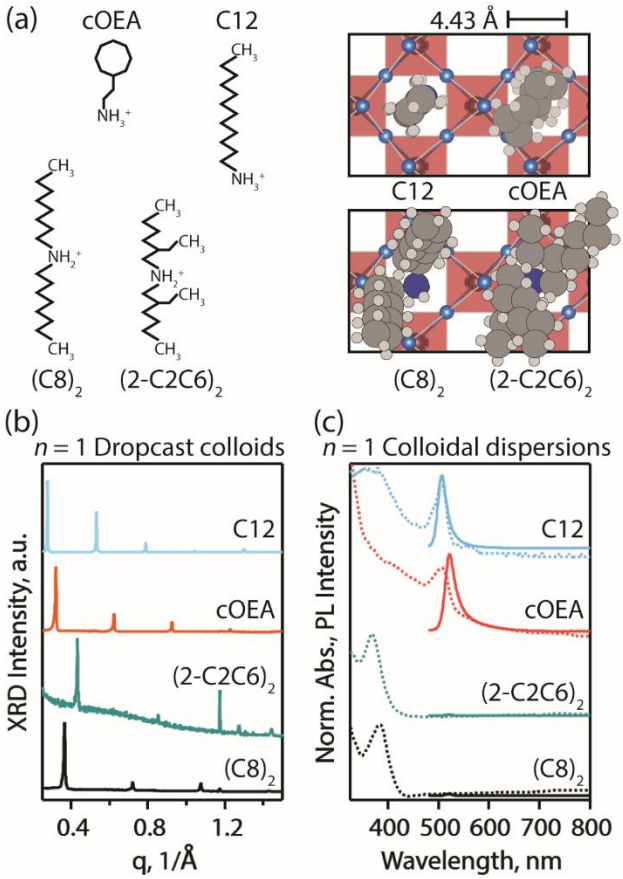

Figure 4. a) Different 'spacer' molecules compared by length and approximate areal packing density with respect to the PbI_x layer surface. b) X-ray diffraction of *n* = 1 phases of drop-cast films

of colloidal perovskites prepared with the alkylammonium species shown in (a). c) PL (solid lines) and absorbance (dashed lines) measurements of dispersions prepared from antisolvent precipitation of n = 1 lead halide R-P phases with different alkylammonium cations. PL spectra were obtained by excitation with 450 nm light.

Competition between spacer and ligand behavior in 2D perovskite colloids. For R-P (or D-J) phases in **Figure 2**, the alkylammonium cations passivate the surface and act as spacers between lead halide layers. If small colloids or nanoparticles are formed, the cations passivating the surfaces must also prevent assembly of 2D perovskite nanocrystals into larger grains. Phase segregation between different *n*-values introduces an additional layer of complexity.[48] Competition between these interactions, either for a single cation or between different species in a mixture of cations, directs the *n*-value and grain size of 2D perovskite colloids. To investigate this effect, we examined competition between three different alkylammonium cations – C4, C12 and cOEA – which can all form R-P phases as spacers but have very different molecular structure.

R-P colloids with a single spacer cation. To begin, $\langle n \rangle$ = 2 colloids prepared with *only* C12, cOEA and C4 spacers were synthesized to compare the optical and structural properties of each single-spacer phase in dispersion. Accurately determining the R-P phase is limited by differences in PL quantum yield of each *n*-value[48,78] or upon aggregation of particles.[37] Colloids prepared with only C4, C12 or cOEA spacers show multi-modal PL that is red-shifted compared to the expected n = 2 R-P phase (**Figure 5**). The size and shape of the spacer affects the *n*-value and phase polydispersity; C12 spacers yield dominant n = 3 PL, while C4 and cOEA spacers show PL dominated by n > 3 phases. Absorbance measurements of the C12 and cOEA colloids show distinct excitonic peaks for n = 2 R-P phases, but shallow band-edges indicate the presence of n > 2 phases. Absorbance scales linearly with volume fraction and can serve as a more reliable estimate of phase distributions than PL. However, for R-P phases absorption cross-section varies significantly with *n*-value because the low-*n* phases have stronger excitonic absorption.[19,86] The absorption data, consistent with PL data, indicates that dispersed $\langle n \rangle$ = 2 colloids prepared with only C4, C12 or cOEA spacers are polydisperse mixtures of R-P phases with different *n*-values.

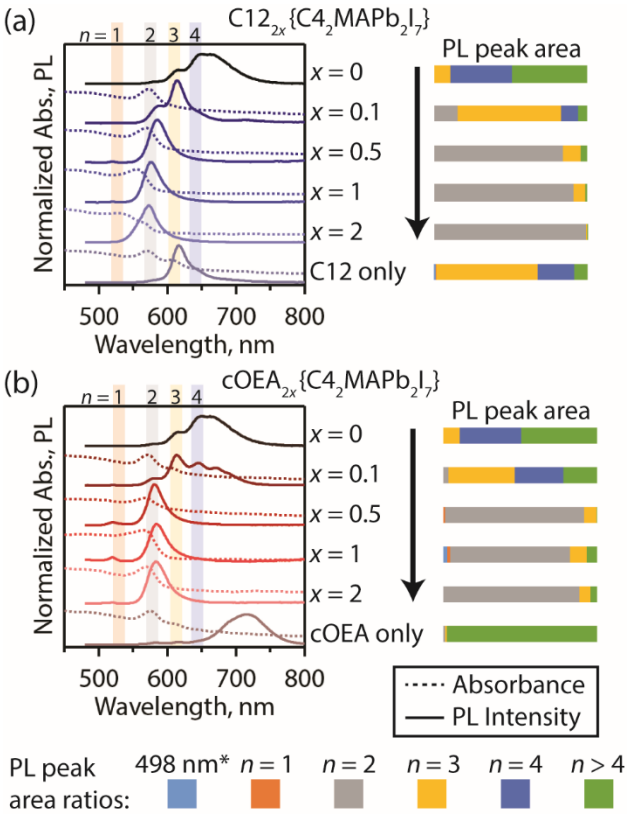

Figure 5. Normalized PL spectra (solid lines) and absorbance spectra (dashed lines) of ~ 0.1 mmol Pb/L colloidal dispersions in toluene prepared with C4, $MAPbI_x$ perovskite precursors and either (a) C12 or (b) cOEA ligands. PL spectra were obtained by excitation with 450 nm light. To test the behavior of added species as 'ligands', insulating cations were added to an <*n*> = 2 precursor mixture of $C4_2MAPb_2I_7$ prior to antisolvent preciptiation for an effective stoichiometry of either a) $C12_{2x}\{C4_2MAPb_2I_7\}$ or b) $cOEA_{2x}\{C4_2MAPb_2I_7\}$. The arrows indicate greater content of added C12 or cOEA species in the precursors. The bar graphs at the right of each plot indicate the fitted Lorentzian peak areas for emission from different *n*-values. The peak at 498 nm (marked with *) is observed in distorted 2D phases of $C12_2PbI_4$.[71]

The influence of spacer composition on colloidal microstructure was investigated by transmission wide-angle X-ray scattering (WAXS) to avoid the challenges posed by optical measurements of dispersed R-P phases. The phase and microstructure of colloidal perovskites can change during dilution or film deposition[39], but X-ray scattering is typically limited to deposited perovskite films or dilute solutions.[36,87] To account for the high X-ray absorption from heavy lead atoms, high-flux synchrotron X-rays were used to measure solutions in quartz capillaries. Integrating the 2D transmission WAXS signal and subtracting out signal from the capillary and toluene background (**Figure S5**) yields clear diffraction patterns of

dispersed crystals, even at high particle loadings (10 mmol Pb/L). The samples measured by transmission WAXS have 100× higher particle concentrations than dispersions in optical measurements shown in **Figure 5**. Unlike grazing-incidence or powder XRD of deposited films,[41,47,54,88] transmission WAXS of dispersions produce powder patterns without grain texturing or preferred orientations from the substrate. Therefore, crystal structures and phase distributions within colloidal samples can be obtained if the structure factors of the phases are known.

Transmission WAXS of dispersed colloids can be indexed to different R-P phases, even without single-crystal reference patterns (**Figure 6**). Single crystal structures of C12- and cOEA-containing R-P phases of higher *n*-value have not been published. Instead, the *n*-value can be estimated from (0*k*0) reflections, which are the only observable diffraction features at q < 1.0 $Å^{-1}$. Unit cells for $n > 1$ phases with C12 and cOEA spacers were estimated from published centrosymmetric n = 1-3 structures of $(C4)_2MA_{n-1}Pb_nI_{3n+1}$.[8] The space group, *a* and *c* parameters were assumed to be identical to $(C4)_2MA_{n-1}Pb_nI_{3n+1}$ for each *n*-value, but the *b* parameter (*i.e.* interlayer spacing) was adjusted based on the interlayer spacing shown in **Figure 3b**. Simulated diffraction patterns of R-P phases matched $\langle n \rangle = 1$ colloidal samples for both dispersions and drop-cast films (**Figure S6**), so we concluded that solvent does not incorporate within the R-P interlayer. Simulated reflections are indicated underneath the diffraction patterns in **Figure 6**, and complete diffraction patterns of all samples are shown in **Figure S11**. Precise atom positions and form factors (*i.e.* diffraction intensity) are unknown for $n > 1$ R-P phases with C12 or cOEA spacers, so only the *d*-spacing for each reflection is shown.

Structural and optical measurements of dispersed $\langle n \rangle = 2$ colloids present inconsistent assignments of *n*-value. The dominant phase observed by transmission WAXS is $n = 2$ for C4 and cOEA spacers, as expected from $\langle n \rangle = 2$ stoichiometry, but C12 spacers form a mixture of $n = 1$ and $n = 2$ phases (**Figure 6**). This result is consistent with XRD of drop cast films of $\langle n \rangle = 2$ C12-only colloids (**Figure 3a**). However, PL and absorbance measurements indicate a distribution of larger *n*-value phases (**Figure 5**). These inconsistencies may be a result of the different sensitivities of optical and diffraction measurements to different R-P phases. Optical measurements require 100× dilution of the stock colloidal dispersion, so particle concentration may also impact the phase distribution. Nonetheless, there is no obvious advantage to using a longer (C12) or sterically-hindered (cOEA) spacer to improve phase purity in single-spacer R-Ps.

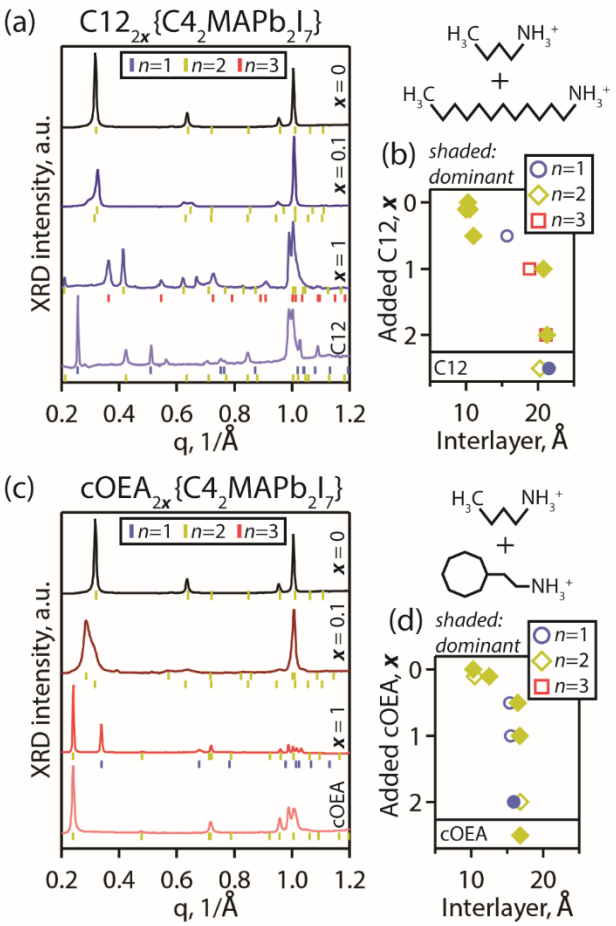

Figure 6. Transmission wide-angle X-ray scattering obtained through 10 mmol Pb/L colloidal dispersions in toluene prepared with C4 spacers, $MAPbI_x$ perovskite precursors and either (a,b) C12 or (c,d) cOEA. Spacer cations were added to an $\langle n \rangle = 2$ precursor mixture of $C4_2MAPb_2I_7$ prior to antisolvent preciptiation for an effective stoichiometry of either $C12_{2x}\{C4_2MAPb_2I_7\}$ (a,b) or $cOEA_{2x}\{C4_2MAPb_2I_7\}$ (c,d). Simulated reflections for the two most dominant phases are shown underneath each measurement corresponding to n = 1,2 or 3 R-P phases with unit cell b parameters adjusted to fit the (0k0) peaks. The plots at the right of each diffraction graph (b,d) indicate estimated interlayer spacings for each of the simulated R-P unit cells.

The spacers direct the size and shape of colloidal grains through surface termination, in addition to the R-P n-value. Colloid morphology determines the stability of dispersions during solution processing and may impact optoelectronic properties of R-P phases. Two complementary techniques are used to observe how different spacers affect colloid particle morphology: peak broadening of transmission WAXS data and transmission small angle neutron scattering (SANS).

The Scherrer broadening equation is used to calculate grain size from transmission WAXS of dispersed R-P particles. We assume no strain broadening effects and negligible instrumental broadening (**Supporting Information**). Dispersed particles are larger than 100 nm along <0*k*0> (*i.e.* the layering dimension, *h*) for C4-only (h > 124 nm), C12-only (h > 107 nm) and cOEA-only (h > 121 nm) compositions (**Figures 7b** and **7c**). Peak broadening is similar for other reflections. For instance, broadening of the (111) n = 2 R-P peak around $q \approx 1$ Å^{-1} in the C4-only <n> = 2 colloid (**Figure 6a**) yields a Scherrer crystallite size of 173 nm, compared to a <0*k*0> dimension of 124 nm (**Table S1**). It is difficult to index non-(0*k*0) peaks without a single crystal pattern for R-P phases with C12 and cOEA spacers. However, none of the peaks in the region expected for R-P (111) reflections ($q \approx 1$ Å^{-1}) exceed full-width half-maxima of 0.025 Å^{-1}, placing a minimum bound of 40 nm on the lateral dimensions of colloidal grains. Thus, colloidal grains are relatively isotropic rather than 1D needles[54] as observed in other reports.[25]

Small angle neutron scattering (SANS) is used to measure the colloidal morphology of dispersed R-Ps. SANS is complementary to grain sizing with WAXS measurements because it can resolve disordered regions or small nanoscale grains that may be unresolvable by Bragg diffraction.[18,20] We optimized contrast for SANS by dispersing R-P colloids in deuterated antisolvent (d-toluene, **Table S3**) at relatively high particle loadings (~ 10 mmol Pb/L), equivalent to the samples measured by transmission WAXS (**Figure 6, Figure S11**). Similar information can be obtained from small-angle X-ray scattering (SAXS),[36] but the high absorption cross-section of Pb and I limits the signal-to-noise ratio.

SANS measurements reveal that extended agglomerates with large colloidal dimensions form in 2D perovskite dispersions. **Figure 7a** shows transmission SANS data from <n> = 2 colloidal dispersions with different amounts of C4, C12 and cOEA spacers. All measured samples have smooth power-law scattering patterns with logarithmic slopes between q^{-3}, indicating dense 3D fractal clusters of particles, and q^{-4}, which indicates sharp interfaces between solvent and solid particles.[89] If the colloidal dispersions were mostly composed of dispersed perovskite nanoplatelets (h < 10 nm), the SANS spectra would look very different, with a much shallower slope at low-q (**Figure S20**). The cOEA-only dispersion shows some evidence of shallower low-q scaling (**Figure 7a**), indicating that cOEA, which is more sterically hindered than C4 or C12, may form smaller particles than C12 or C4. WAXS broadening of cOEA-only samples does not indicate that smaller crystallites form for cOEA spacers, and this apparent contradiction may indicate limitations due to particle polydispersity, morphology or measurement uncertainty. Nonetheless, none of the cations are observed to exfoliate individual R-P nanoplatelets in solution at these concentrations. Dilution of the dispersed colloids up to 100× did not have a noticeable effect on the SANS spectra, aside from diminishing the total scattering signal (**Figure S21**). This indicates that the upturn in scattering

intensity at $q < 0.1$ Å^{-1} is not concentration dependent (*i.e.*, dense fractal clusters of particles form regardless of the concentration).

R-P colloids with mixtures of alkylammonium spacers. Competition between different cations in mixtures of alkylammonium spacers was investigated as a means to control *n*-value and grain morphology in R-P colloids. Mixed alkylammonium compositions (*e.g.* C4 and C8, or C4 and C12) have been observed to improve the colloidal stability (*i.e.* by decreasing colloid grain size) and phase purity of antisolvent precipitated 2D perovskite colloids.[68] It is challenging to directly determine which spacers are present within the interlayer or at the surface of colloidal particles, but indirect evidence such as particle size, quantum phase and XRD spacing can be used to infer these relationships.

We examined the competition between different spacer molecules by varying the relative composition of C4 and either C12 or cOEA within precursor solutions for a composition of $(R)_{2x}\{C4_2MAPb_2I_7\}$. cOEA and C12 species were treated as 'additives' to an effective $\langle n \rangle = 2$ C4 R-P stoichiometry (see **Figure S1** for explanation). **Figure 5** shows PL and absorbance spectra for colloidal dispersions prepared from precursors with compositions of $(R)_{2x}\{C4_2MAPb_2I_7\}$, where *R* represents either cOEA or C12. As greater concentrations of C12 or cOEA are added, the PL spectra blue-shift (suggesting a lower *n*-value) and appear to become more phase-pure (**Figure 5a,b**). Adding an excess of larger C12 or cOEA spacers ($x = 2$) forms colloids that show PL dominated by the $n = 2$ phase (580 nm). This result is consistent with earlier reports of C12 as an effective additive to generate stable colloidal dispersions of phase-pure $n = 2$ 2D perovskites.[38] More generally, colloids with lower *n*-value PL and XRD characteristics can be formed by adding an excess of spacers.[68] The *n*-value would decrease if added C12 or cOEA species can act as spacers (*R*), creating R-P phases with a stoichiometry of $\{R\text{:}C4\}_2MA_{n-1}Pb_nI_{3n+1}$. If C12 or cOEA only behaved as surface ligands for R-P colloids composed of C4 spacers, the *n*-value would not decrease with added C12 or cOEA. Higher-energy exciton peaks and above-gap absorbance both increase in intensity as more C12 or cOEA is added (**Figure 5**). Thus, adding C12 or cOEA alongside C4 yields an excess of spacer molecules to stabilize lower *n*-value phases in the dispersion.

Transmission WAXS of colloids with mixed spacers reveals a distribution of R-P *n*-values that is sensitive to spacer composition. The interlayer distance can fluctuate if spacers alloy between layers. Therefore, *n*-values were assigned so the fitted interlayer distance was bounded by the lower limit of C4-only phases ($d \sim 10$ Å) and upper limit of either C12-only ($d \sim 21$ Å) or cOEA-only ($d \sim 17$ Å) R-P phases (**Figure 3b**). It is conceivable that methylammonium (MA) could also alloy within the interlayer, but we did not observe reasonable phase assignments with interlayer distances less than ~10 Å (C4-only). For most mixtures of added spacers (C4 and C12, or C4 and cOEA), an $n = 2$ R-P phase is dominant (**Figure 6**). The

only exceptions are C12-only and x = 2 cOEA, which are mostly n = 1 alongside weaker n = 2 phases. It is expected that adding excess spacers (C12 or cOEA) will stabilize lower n-value phases if C12 and cOEA incorporate between R-P layers (**Figure 5**). This trend is observed for added cOEA (**Figure 6**), but excess C12 causes an unexpected occurrence of n = 3 phases for larger concentrations of C12 (x = 1, 2). We note that some peaks are unassigned for C12 transmission WAXS patterns, and phase designations may be ill-defined due to structural distortions and polydispersity. There are also clear inconsistencies between optical and WAXS assignments of R-P phases with mixed spacers. Colloids prepared with only a small addition of C12 or cOEA (x = 0.1) show multi-modal PL and absorbance (**Figure 5**), whereas transmission WAXS only indicates n = 2 phases (**Figure 6**). As described previously, this may be attributed to the sensitivities of each technique to different n-values, or changes in structure upon 100× dilution for optical measurements.

Colloids prepared from cation mixtures with a substitutional stoichiometry have phase and structural properties that are sensitive to the choice of shorter and longer alkylammonium cations. Substituting C4 with C12 or cOEA retains the absolute ratio between alkylammonium ions and $MAPbI_3$ precursors (see **Figure S1**). In this scheme, the precursor composition is $(R_yC4_{1-y})_2MAPb_2I_7$. There is no clear blue-shifting in the average emission and absorption of particles upon increased y (*i.e.* more C12 or cOEA) for either species (**Figure S10**). This result is expected if all three species can act as spacers because the average $\langle n \rangle$ stoichiometry doesn't change with y. However, there are changes in phase purity and dispersion stability with ligand content. Colloids with substituted C12 spacers, which have similar steric arrangements to C4, have predominant n = 3 emission, along with emission from n = 2 and n > 3 phases (**Figure S10a**). The phase purity seems to be highest for an intermediate composition of mixed C4 and C12 (y = 0.5). PL and absorbance of substitutionally-mixed C4 and cOEA, which do not share common steric arrangements, indicate phase segregation into low-n (n = 2, 3) and high-n (n > 3) phases as cOEA content is increased (**Figure S10b**). However, only n = 2 phases are observed by WAXS for cOEA mixtures (**Figure S11d, S12b**). Despite the inconsistency between optical and WAXS measurements, it is clear that C12 and cOEA have different impacts on n-value polydispersity in substitutional mixtures.

Previous studies of spin-coated R-Ps have suggested that small domains of $MAPbI_3$ form during growth, causing anomalous low-energy emission in polydisperse films.[18,20] This hypothesis is a possible explanation for the broad low-energy feature in the $\langle n \rangle$ = 2 cOEA-only dispersion (**Figure 5**), or substitutional mixtures with high cOEA contents (**Figure S10b**). **Figure S7** compares transmission WAXS to simulated $MAPbI_3$ and $C4_2MAPb_2I_7$ XRD powder patterns. Characteristic (002) and (110) reflections for $MAPbI_3$ around $q \approx 1.0$ Å^{-1}, and (004) and (220) reflections around $q \approx 2.0$ Å^{-1}, are not observed with identical peak intensities and locations in transmission WAXS of R-P dispersions. Thus, the low energy

emission (> 700 nm) observed in some R-P dispersions (**Figure 6, Figure S10**) is either due to higher *n*-value R-P phases or small $MAPbI_3$ domains that cannot be resolved by XRD.

Diffraction measurements of dispersed NCs with mixed C12 and C4 spacers indicate that linear alkylammonium molecules can mix within 2D perovskite interlayers. The estimated interlayer spacing for each phase is shown beside the diffraction patterns in **Figure 6b,** ranging from about 10 Å for C4-only to about 21 Å for C12-only. Interlayer distance is distinct from the distribution of *n*-values in R-P phases. For instance, the C12-only sample shows polyphasic diffraction (**Figure 6b**) from various *n*-values, but the interlayer separation is nearly identical for each phase. The composition of the interlayer can be inferred by measuring the interlayer separation. If the spacer is predominantly C4 (x = 0.1) or C12 (x = 2.0), the interlayer spacing is similar to C4-only or C12-only R-Ps, respectively (**Figure 3a, Figure 6b, Figure S11a**). However, the interlayer separation lies between C4-only and C12-only distances for intermediate (x = 0.5, 1.0) mixtures (**Figure 6b, Figure S11a**). Similar results are observed for a substitutional stoichiometry of mixed C4 and C12 (**Figure S11c**, **S12a**). Intermediate interlayer spacings have also been observed in mixed spacer compositions for spin-cast $MAPbBr_3$-based R-P films and n = 1 R_2SnI_4 R-P phases,[90,91] but the interlayer structure of layered perovskites with mixed spacer cations remains unclear. We find that the interlayer spacing is determined by the atomic density of methylene units between lead halide sheets (**Figure 3**), rather than pillaring due to the outstretched length of spacers. Thus, the intermediate interlayer spacing of colloids with mixed C4 and C12 indicates that these spacers are mixed within the crystalline interlayers of colloidal R-P phases.

Unlike C12, cOEA phase segregates from C4 spacers within 2D perovskite interlayers. At intermediate cOEA contents (x = 0.5, 1, 2) two clear diffraction patterns can be distinguished (**Figure 6d, Figure S11b**). One pattern corresponds to the n = 2 phase for R-Ps with only cOEA spacers (the reflections at q = 0.24, 0.48, 0.72 $Å^{-1}$). The other pattern matches cOEA-only n = 1 R-P phase (q = 0.34, 0.68, 1.02 $Å^{-1}$). The n = 1 phase becomes more dominant as excess cOEA lowers the average stoichiometry to smaller $\langle n \rangle$ (**Figure 6d, Figure S11b**). cOEA does not share common steric arrangements with C4. Thus, alloying between cOEA and C4 is less favorable than between mixed linear alkylammonium species. There are no signatures of C4-containing R-P phases by transmission WAXS even for x = 0.5, which represents a 2:1 ratio of C4:cOEA. Similar results are observed for a substitutional stoichiometry, and even a small amount of substituted cOEA (y = 0.3, C4:cOEA ~ 2:1) can completely exclude C4 from R-P crystallization (**Figure S11d, S12b**). However, spacer alloying can occur if only a small amount of cOEA is present. An intermediate diffraction peak corresponding to an interlayer spacing of 13 Å is found between the interlayer spacings of n = 2 cOEA (17 Å) and C4 (10 Å) for x = 0.1 (**Figure 6d**). Diffraction peaks for x = 0.1 of

added cOEA, or $y = 0.1$ of substituted cOEA, are very broad, suggesting that smaller crystallites form with alloyed cOEA and C4 spacers.

Competition between mixed spacers controls particle size independently of the *n*-value or interlayer separation. R-P $\langle n \rangle = 2$ colloids prepared with a single spacer (C4-only, C12-only and cOEA-only) show similar WAXS peak broadening ($h > 100$ nm) regardless of the spacer (**Figures 6b,c, S8, S9**). However, adding a small amount of C12 or cOEA ($x = 0.1$) to $\{C4_2MAPb_2I_7\}$ precursors during growth decreases particle size for both added C12 ($h > 59$ nm) and cOEA ($h > 41$ nm). Adding a larger excess ($x = 1.0$) of C12 or cOEA to $\{C4_2MAPb_2I_7\}$ has the opposite effect; larger particles form for added C12 ($h > 195$ nm) and cOEA ($h > 190$ nm). These trends, which are independent of interlayer spacer alloying or R-P *n*-value, are qualitatively confirmed by SANS measurements (**Figure 7a**). Colloids prepared with small amounts of added C12 or cOEA ($x = 0.1$) show a transition in the SANS scaling from $\sim q^{-4}$ at larger q (*i.e.* sharp interfaces between solid particles and solvent) to low-q scaling closer to q^{-3} (*i.e.* dense fractal clusters of smaller particles). The transition between these scaling regimes for $x = 0.1$ occurs around $q \sim 0.01$ Å^{-1} (~ 60 nm in real space). Larger particles ($h > 100$ nm) would show a transition from solid particles with sharp interfaces (q^{-4}) to dense fractal clustering (q^{-3}) at lower q values, beyond the resolution of the SANS measurement, yielding the $\sim q^{-4}$ scaling observed for mixtures with large excesses ($x = 1.0$) of added C12 or cOEA. Both SANS and WAXS indicate that colloidal particle sizes decrease if a small amount of longer cations are added, but adding a larger excess of C12 or cOEA increases particle size. Thus, the balance between surface-terminating 'ligand' behavior and interlayer 'spacer' behavior of C12 and cOEA depends on the relative concentrations of each cation in solution.

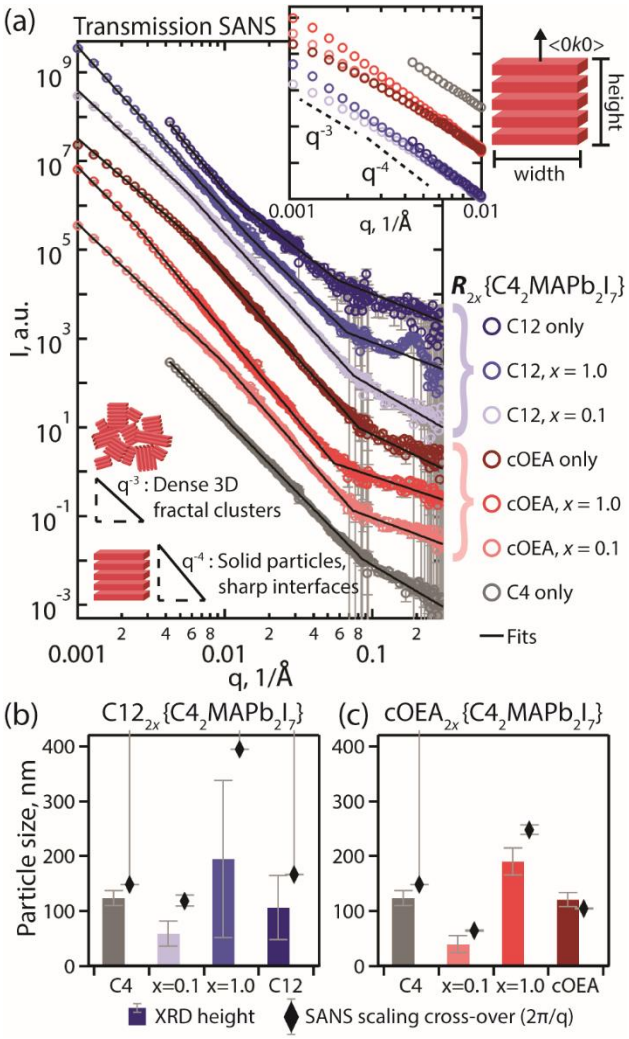

Figure 7. a) Transmission small angle neutron scattering (SANS) patterns from ~ 10 mmol Pb/L colloidal dispersions in deuterated toluene prepared with C4 spacers, $MAPbI_x$ perovskite precursors and added C12 or cOEA. SANS patterns are offset by a constant multiplicative factor for easier comparison of the data. The inset shows the low-*q* region of the same data to highlight differences in scaling. Fits of the SANS data to an empirical three power law model are shown as solid black lines. Particle sizes estimated from transmission WAXS measurements and fits of the SANS data are compared for R-P mixtures with added b) C12 or c) cOEA cations.

SANS data were fit to an empirical three power law model to quantify particle morphology. This model links three distinct power law scalings (*i.e.* $I(q) = Aq^{-m}$, where A is a constant prefactor and m is the power law exponent, **Supporting Information**) across the entire SANS spectrum:

Three power law model: $$I(q) = \begin{cases} Aq^{-m_1} \; ; \; q \leq q_{c,1} \\ Bq^{-m_2} \; ; \; q_{c,1} < q \leq q_{c,2} \\ Cq^{-m_3} \; ; \; q > q_{c,2} \end{cases}$$

The transition from q^{-4} scaling (*i.e.* sharp interfaces between solid particles) to shallower scaling at lower q values (*i.e.* dense fractal clusters of smaller particles) depends on the size of R-P grains. The q value of this transition, $q_{c,1}$, can be used to estimate particle morphology as size ~ $2\pi/q_{c,1}$. **Figure 7a** shows fits of each SANS pattern to a model of three power law scaling relationships. Some of the SANS patterns do not show a transition from ~q^{-4} scaling to ~q^{-3} scaling within instrumental limits (C4 only, C12 only, C12 x = 1.0), so the smallest measured q value is a lower bound on particle sizes for these colloids. Parameters obtained from these fits are illustrated in **Figure S17** and tabulated in **Table S2**. Particle sizes estimated by SANS fits are compared to grain sizes estimated from WAXS measurements in **Figures 7b** and **7c**. Estimated particle sizes are consistent between SANS and WAXS measurements; smaller particles form when a small amount of C12 or cOEA is added (x = 0.1), while larger excesses of C12 or cOEA, or single spacer cation mixtures, yield larger particles.

SANS measurements were also fit to physical models based on more realistic descriptions of particle structure, but the coarseness of the data limits the information we can obtain. **Figure S18** compares fits to four different models: the empirical three power law model and models of dispersed cylinders, parallelepipeds, and stacked disks. Details for each model are described in the **Supporting Information**. The cylinder and parallelepiped models do not fit the SANS data across the entire range of q values (**Figure S18**). The stacked disk model captures the layered structure of R-Ps, and has been used for other hybrid organic-inorganic layered materials such as montmorillonite.[92] Fits with the stacked disk model, using particle 'heights' (**Figure 2**) estimated from WAXS as inputs and significant polydispersity in grain dimensions, capture the correct scaling (q^{-m}) of the measured SANS patterns, and how this scaling varies with q (**Figure S19** and **Table S4**). These fits are consistent with dispersions of polydisperse colloidal particles that are roughly 100 nm in stacking and lateral dimensions, rather than isolated nanoplatelets. However, the fits include peaks and shoulder-like features that are distinct from the observed, smooth power-law scaling of the measurements. Lateral particle dimensions estimated from the stacked disk model range from 78 nm (cOEA x = 1.0) to 768 nm (cOEA only), and do not show systematic relationships to stoichiometry or sizes obtained from the three power law fits and WAXS analysis (**Table S4**). The SANS data are too coarse for the stacked disk model to distinguish between different cation mixtures, so we rely on fits to the empirical three power law model instead. Nonetheless, if a significant fraction of nuclei were present as isolated nanoplatelets, a distinct hump would be expected in the mid-q range (**Figure S20e**). The

lack of such a feature indicates that exfoliated nanoplatelets, if present, make up a minority (< 10%) of the colloidal material.

The effects of competition between mixed cations, behaving either as ligands or spacers, can be summarized by comparing the optical, WAXS and SANS measurements of R-P colloids prepared from ternary cation mixtures. Two regimes are revealed from trends in particle size (**Figure 7b,c**), interlayer spacing (**Figure 6**) and optical properties (**Figure 5**). If only a small amount of C12 or cOEA is added (x = 0.1) to {$C4_2MAPb_2I_7$} precursors, optical emission is polydisperse among different n-values, the interlayer separation is closer to C4-only R-P phases, and smaller colloidal grains form. Thus, C12 or cOEA mostly act as ligands in low concentrations, stabilizing smaller R-P colloids. If more C12 or cOEA is added, larger particles form with improved phase purity by optical measurements. The density of the interlayer is similar to polyethylene across all tested alkylammonium spacers (**Figure 3**), but interactions between different spacers change how they mix. If sufficient C12 is added (x > 0.1) to {$C4_2MAPb_2I_7$}, an alloy of C12 and C4 forms between R-P layers, but adding sufficient cOEA (x > 0.1) instead forms segregated domains that exclude C4 from the interlayer. Interactions between different spacers also direct the phase and morphology of R-P colloids. The favorable mixing between linear alkylammonium cations, which share common steric arrangements, may explain why optical phase purity (*i.e.* n-value) is greater in substitutional mixtures of C4 and C12 than C4 and cOEA (**Figure S10**); there is less impetus for the precursors to segregate into polydisperse phases.

The important role of the solvent in balancing the competition between ligand and spacer behavior in ternary cation mixtures is demonstrated by depositing colloidal perovskites into drop-cast films. **Figures S13-S16** compare the WAXS and optical absorbance of dispersed and drop-cast perovskite colloids with mixed C4 and C12 or C4 and cOEA spacers. Drop-cast films show continuous changes in d-spacing of low q (0k0) R-P reflections with the amount of added or substitutional C12 or cOEA. Thus, the interlayer spacing between lead iodide octahedral sheets changes continuously with the average spacer composition in drop-cast films of colloidal perovskites. This result is very different from diffraction observed in dispersed colloids, which are segregated between R-P phases with distinct interlayer separations (**Figure 6, Figure S11, S12**). Optical absorbance does not show clear differences between dispersed and drop-cast colloids (**Figures S13b-S16b**), so the n-value distribution may not be as sensitive to solvent (toluene) as the interlayer structure during growth. The common linear structure of C4 and C12, or steric hindrance of cOEA spacers, seems to be less impactful to R-P crystal growth in the absence of solvent.

Conclusion

Control over the microstructure of colloidal 2D perovskites requires a distinction between the cations that separate perovskite layers, and terminating ligands that define the boundaries of 2D perovskite grains in solvent. We determined that crystalline 2D perovskite colloids can form from a wide range of alkylammonium spacers, with structural properties that are indistinguishable from R-P crystals for a variety of alkylammonium species with linear and branched structures. Alkylammonium spacers pack with constant methylene density in the R-P interlayer regardless of length or branching, and exclude interlayer solvent in dispersed colloids. WAXS and SANS of colloidal dispersions revealed that large (~ 100 nm) crystalline grains form, with dimensions that can be tuned by spacer composition. Mixing C4 and longer alkylammonium spacers with either linear (C12) or cyclic (cOEA) structures induces changes in quantum well thickness, interlayer structure and colloidal size. Mixed linear spacers (*i.e.* C12 and C4) lead to alloyed interlayer structures and with tunable phase purity. However, mixing C4 and the cyclic spacer, cOEA, segregates cOEA-only R-P grains from C4 spacers, and has complex effects on phase distributions in solution. Adding just a small amount of either cOEA or C12 to $C4_2MAPb_2I_7$ forms the smallest colloidal particles, but at the expense of polydisperse interlayer structures and *n*-values. Phase fractions of different *n*-values diverge between XRD and optical measurements, revealing that quantitative comparisons of phase fraction between these techniques, and across different particle concentrations, is challenging.

The structure of colloidal 2D perovskites is determined by a sensitive balance between spacer-spacer and spacer-solvent interactions, and future synthetic progress for solution-processed 2D perovskites requires a careful accounting of these phenomena. More generally, we demonstrate that the interlayer region of layered 2D perovskites is responsive to solvent-mediated mixing behavior among different insulating cations. These results suggest that the molecular design of spacer cations and solution processing techniques can be used to engineer the growth of layered perovskites.

Experimental Methods

Materials. Precursor chemicals were purchased from commercial suppliers when possible, including methylammonium iodide (Greatcell Solar), butylammonium iodide (Greatcell Solar), octylammonium iodide (Greatcell Solar) and lead iodide (99%, Sigma Aldrich). The solvents described in the manuscript were anhydrous *N*,*N* – dimethylformamide (DMF) (99.8%. Sigma Aldrich), toluene (99.9%, Fisher), and diethyl ether (99.0%, Millipore). To prepare certain ammonium iodide salts, amine precursors were reacted

with hydroiodic acid (57 wt % in water, Sigma Aldrich) as described below. The amine precursors were hexylamine (99%, Sigma Aldrich), dodecylamine (98%, Sigma Aldrich), octadecylamine (97%, Sigma Aldrich), dioctylamine (97%, Sigma Aldrich), bis-(2-ethylhexyl)amine (99%, Sigma Aldrich) and 2-cyclooctylethylamine (Sigma Aldrich). All ammonium iodide salts and DMF were stored in a nitrogen glovebox.

Synthesis of ammonium iodide spacers. The ammonium iodide spacers that were not purchased from commercial suppliers were synthesized from amine precursors. Ammonium iodide salts were synthesized by dissolving the corresponding amine in ethanol at a concentration of 1.2 M and immersing the container in a water bath at ambient conditions. A slight molar excess of hydroiodic acid was added dropwise to the amine and ethanol solution while stirring to convert the amine to ammonium iodide, and the reaction was allowed to proceed for an hour. The reaction was performed in a fume hood with the sash lowered to avoid hazards from splashing or vapor evolution. Water and ethanol in the reacted product were removed by rotary evaporation. The resulting precipitate was washed many times by adding diethyl ether, stirring the mixture, and decanting to remove residual hydroiodic acid and triiodide, which has a noticeable red color. This process was repeated until the supernatant ether only had a faint yellow color and the precipitate ammonium iodide salt was a homogeneous white color. The washed ammonium iodide was then dried at 60°C under vacuum overnight and transferred to a nitrogen glovebox for storage.

Synthesis of $cOEA_2PbI_4$. Large crystals of $cOEA_2PbI_4$ were prepared following similar methods to other alkylammonium lead iodide Ruddlesden-Popper phases.[8] An amount of 223 mg (1 mmol) of 99.9% PbO powder was dissolved in 5 mL of hydroiodic acid and 1 mL of hypophosphorous acid solution by heating under stirring for 5–10 min at ∼130 °C until the solution turned clear bright yellow. 0.5 mL of hydroiodic acid was added to 282 mg (1 mmol) of 2-cyclooctyl-ethylammonium iodide in a separate vial under stirring. Small orange plate-like crystals precipitated immediately upon combining the above two vials.

Antisolvent precipitation of colloidal perovskites. 2D perovskite colloids were synthesized by antisolvent precipitation following established techniques.[68,93] Precursor solutions were prepared by mixing ammonium iodide and lead iodide salts in DMF at ratios to match the stoichiometry of R-P phases with different spacers, *R* ($R_2MA_{n-1}Pb_nI_{3n+1}$). Precursors solutions with mixtures of butylammonium (C4) and other spacers were prepared with stoichiometries defined by either by adding ($R_{2x}C4_2MA_{n-1}Pb_nI_{3n+1}$) or substituting ($\{R_yC4_{1-y}\}_2MA_{n-1}Pb_nI_{3n+1}$) different spacers for C4. All precursor solutions were prepared with [Pb] = 0.5 M in a nitrogen glovebox, and used within two weeks to avoid effects due to colloidal nucleation and growth of lead iodide within precursor solutions.[38] Colloidal perovskite dispersions were prepared by

rapidly adding 50 µL of precursor solutions to 10 mL of toluene in a 20 mL scintillation vial while stirring in ambient conditions. The mixture quickly changed color depending on the composition of the precursor solution. The mixture was allowed to stir for 10 min in ambient conditions. Afterwards, the solution was centrifuged at 9000 RPM for 10 min to precipitate the perovskite colloids. The supernatant was discarded to remove residual DMF, and the dried pellet was redispersed in 1.5 mL of toluene by sonication. The resulting dispersion was centrifuged, the supernatant was discarded and the precipitate was redispersed in 1.5 mL (~10 mmol Pb/L) for a second washing step. All measurements (Absorbance, PL, WAXS, SANS) were obtained within a day of synthesis to avoid agglomeration and degradation of the perovskite colloids.

Drop-cast film deposition. Drop-cast films were prepared by dropping ~50 µL of colloidal dispersions in toluene (~10 mol Pb/mL) on 1.5 cm × 1.5 cm quartz substrates in ambient conditions and allowing the solvent to evaporate. Prior to deposition, substrates were washed by sequential baths in distilled water, acetone and isopropanol during sonication. Immediately prior to solution drop-casting the substrates were exposed to a 10 min plasma cleaning treatment to improve solvent wetting on the substrate.

Optical measurements. Optical measurements of colloidal dispersions and drop-cast thin films were performed in ambient conditions. UV-Vis absorbance was measured using a Shimadzu UV-2600 ultraviolet-visible spectrophotometer at room temperature in ambient conditions, baselined to a bare quartz substrate. An integrating sphere was used to capture all scattered light transmitted through the film to account for film roughness. Photoluminescence measurements were performed on a Horiba FluoroMax 4 spectrometer calibrated using Milli-Q water**.** Absorbance and photoluminescence of dispersions were measured through a capped 1 cm path-length quartz cuvette and baselined to the empty instrument background. Films were loaded into a thin film sample stage with the substrate oriented at a 20˚ angle of incidence to remove scattering effects. All measurements were performed with an excitation wavelength of 450 nm. In order to limit the effects of Rayleigh scattering at long wavelengths, a long-pass filter slightly above the excitation wavelength (455 nm) was placed in front of the emission port.

Powder X-ray diffraction. Specular X-ray diffraction measurements were performed on a Panalytical Empyrean powder diffractometer with a Cu-Kα source operating with an accelerating voltage of 45 kV and a beam current of 40 mA. Samples were rotated during collection to improve signal-to-noise.

Synchrotron wide angle X-ray scattering. Wide angle X-ray scattering measurements in both transmission and grazing-incidence (GIWAXS) modes were performed at beamline 11-3 at the Stanford Synchrotron Radiation Lightsource (SSRL). The beam energy at the end station is 12.7 eV and the beam spot size is approximately 0.05 mm in the horizontal direction and 0.15 mm in the vertical direction.

Measurements were collected with a 2D Rayonix MX225 CCD detector. The source-to-detector distance, approximately 315 mm, was calibrated using a standard sample of lanthanum hexaborate (LaB_6). For all GIWAXS measurements, a grazing incidence angle of 1.0° was used to eliminate peak doubling observed at smaller incidence angles in thicker drop-cast film samples. The beam height was calibrated to the top surface of a glass substrate prior to deposition. Transmission WAXS was collected of NC dispersions by placing a quartz capillary in the beam path and adding NC dispersions at an effective concentration of ~10 mol Pb/mL. For reference, this is the concentration used in SANS experiments (**Figure 7**), and is similar to a dense film that is 2 – 3 μm thick, in terms of the attenuation of X-rays through a NC sample. All raw GIWAXS images were processed using the Nika software suite,[94] and geometrically corrected using WAXStools.[95]

Small angle neutron scattering. Small angle neutron scattering (SANS) measurements were performed at the NIST Center for Neutron Research on the NGB 30 m SANS instrument. Data were collected at four detector configurations to span the desired q range (0.003 to 0.4 Ang−1) using a wavelength of $\lambda = 8.4$ Ang and $\Delta\lambda/\lambda = 0.11$ at a detector distance of 13.5 m and a wavelength of $\lambda = 6$ Ang and $\Delta\lambda/\lambda = 0.11$ at detector distances of 1, 4, and 13.5 m. The samples were loaded into titanium scattering cells sandwiched between two quartz windows (1 mm pathlength) for SANS measurement. Measurements were made at room temperature in rotating cells to prevent aggregates from settling. SANS data were reduced using the NCNR IGOR software package and analyzed using the SasView software package.[96]

Supporting Information

The Supporting Information is available free of charge on the ACS Publications website.

Detail about colloidal precursor stoichiometry, geometrical approximations of layered perovskite structure from powder XRD, raw transmission XRD of dispersed colloids to show experimental background scattering, additional PL spectra of colloids prepared with different spacers, expanded powder XRD patterns of dispersed colloids, films and ground single crystals of the precursor compositions discussed in the manuscript, Williamson-Hall plots and Scherrer analysis results to estimate grain sizes from transmission XRD of colloids, PL, absorbance and XRD measurements of colloids prepared with a substitutional stoichiometry of mixed cations, PL, absorbance and XRD comparing deposited films of colloids to dispersed colloids with different spacer compositions, more detail about SANS fitting and a

comparison of different scattering models, simulations and discussion of the stacked disk model of SANS, SANS spectra for colloids upon dilution to compare the effects of particle concentration.

Acknowledgments

Materials synthesis and structural characterization were supported by the U.S. Department of Energy, Office of Science, Basic Energy Sciences, under Award Number DE-SC-0012541. Use of the Stanford Synchrotron Radiation Lightsource, SLAC National Accelerator Laboratory, is supported by U.S. Department of Energy, Office of Science, Basic Energy Sciences under Contract No. DE-AC02-76SF00515. Access to the NGB30M SANS instrument was provided by the Center for High Resolution Neutron Scattering, a partnership between the National Institute of Standards and Technology and the National Science Foundation under agreement no. DMR-1508249. We acknowledge the support of the National Institute of Standards and Technology, U.S. Department of Commerce, in providing the neutron research facilities used in this work. We also thank Dr. Yun Liu from NIST Center for Neutron Research for assistance performing neutron scattering experiments. This work benefited from the use of the SasView application, originally developed under NSF Award DMR-0520547. SasView contains code developed with funding from the European Union's Horizon 2020 research and innovation programme under the SINE2020 project, grant agreement No 654000. The research reported here also made use of the shared facilities of the UCSB MRSEC (NSF DMR 1720256), a member of the Materials Research Facilities Network (www.mrfn.org). R. M. K. gratefully acknowledges the National Defense Science and Engineering Graduate Fellowship for financial support. The authors thank Tanvi Sheth, Serena Seshadri and Tuan Nguyen for assistance with exploratory experiments and helpful discussion.

ORCID IDs:

Clayton J. Dahlman: 0000-0002-4555-4846

Naveen R. Venkatesan: 0000-0003-2086-5274

Patrick T. Corona: 0000-0002-6829-9366

Rhys M. Kennard: 0000-0003-1181-5638

Lingling Mao: 0000-0003-3166-8559

Noah C. Smith: 0000-0002-4150-2387

Jiamin Zhang: 0000-0003-2982-3417

Ram Seshadri: 0000-0001-5858-4027

Matthew E. Helgeson: 0000-0001-9384-4023

Michael L. Chabinyc: 0000-0003-4641-3508

References

(1) Snaith, H. J. Present Status and Future Prospects of Perovskite Photovoltaics. *Nat. Mater.* **2018**, *17*, 372–376.

(2) Zhang, W.; Eperon, G. E.; Snaith, H. J. Metal Halide Perovskites for Energy Applications. *Nat. Energy* **2016**, *1*, 16048.

(3) Brenner, T. M.; Egger, D. A.; Kronik, L.; Hodes, G.; Cahen, D. Hybrid Organic-Inorganic Perovskites: Low-Cost Semiconductors with Intriguing Charge-Transport Properties. *Nat. Rev. Mater.* **2016**, *1*, 15007.

(4) Berry, J.; Buonassisi, T.; Egger, D. A.; Hodes, G.; Kronik, L.; Loo, Y.-L.; Lubomirsky, I.; Marder, S. R.; Mastai, Y.; Miller, J. S.; Mitzi, D. B.; Paz, Y.; Rappe, A. M.; Riess, I.; Rybtchinski, B.; Stafsudd, O.; Stevanovic, V.; Toney, M. F.; Zitoun, D.; Kahn, A.; *et al*. Hybrid Organic-Inorganic Perovskites (HOIPs): Opportunities and Challenges. *Adv. Mater.* **2015**, *27*, 5102–5112.

(5) Snaith, H. J. Perovskites: The Emergence of a New Era for Low-Cost, High-Efficiency Solar Cells. *J. Phys. Chem. Lett.* **2013**, *4*, 3623–3630.

(6) Quan, L. N.; Yuan, M.; Comin, R.; Voznyy, O.; Beauregard, E. M.; Hoogland, S.; Buin, A.; Kirmani, A. R.; Zhao, K.; Amassian, A.; Kim, D. H.; Sargent, E. H. Ligand-Stabilized Reduced-Dimensionality Perovskites. *J. Am. Chem. Soc.* **2016**, *138*, 2649–2655.

(7) Tsai, H.; Nie, W.; Blancon, J.-C.; Stoumpos, C. C.; Asadpour, R.; Harutyunyan, B.; Neukirch, A. J.; Verduzco, R.; Crochet, J. J.; Tretiak, S.; Pedesseau, L.; Even, J.; Alam, M. A.; Gupta, G.; Lou, J.; Ajayan, P. M.; Bedzyk, M. J.; Kanatzidis, M. G.; Mohite, A. D. High-Efficiency Two-Dimensional Ruddlesden–Popper Perovskite Solar Cells. *Nature* **2016**, *536*, 312–316.

(8) Stoumpos, C. C.; Cao, D. H.; Clark, D. J.; Young, J.; Rondinelli, J. M.; Jang, J. I.; Hupp, J. T.; Kanatzidis, M. G. Ruddlesden–Popper Hybrid Lead Iodide Perovskite 2D Homologous Semiconductors. *Chem. Mater.* **2016**, *28*, 2852–2867.

(9) Cao, D. H.; Stoumpos, C. C.; Farha, O. K.; Hupp, J. T.; Kanatzidis, M. G. 2D Homologous Perovskites as Light-Absorbing Materials for Solar Cell Applications. *J. Am. Chem. Soc.* **2015**, *137*, 7843–7850.

(10) Smith, I. C.; Hoke, E. T.; Solis-Ibarra, D.; McGehee, M. D.; Karunadasa, H. I. A Layered Hybrid Perovskite Solar-Cell Absorber with Enhanced Moisture Stability. *Angew. Chem.* **2014**, *126*, 11414–11417.

(11) Saparov, B.; Mitzi, D. B. Organic–Inorganic Perovskites: Structural Versatility for Functional Materials Design. *Chem. Rev.* **2016**, *116*, 4558–4596.

(12) Smith, M. D.; Connor, B. A.; Karunadasa, H. I. Tuning the Luminescence of Layered Halide Perovskites. *Chem. Rev.* **2019**, *119*, 3104–3139.

(13) Mao, L.; Stoumpos, C. C.; Kanatzidis, M. G. Two-Dimensional Hybrid Halide Perovskites: Principles and Promises. *J. Am. Chem. Soc.* **2018**, *141*, 1171–1190.

(14) Grancini, G.; Nazeeruddin, M. K. Dimensional Tailoring of Hybrid Perovskites for Photovoltaics. *Nat. Rev. Mater.* **2019**, *4*, 4.

(15) Soe, C. M. M.; Nagabhushana, G. P.; Shivaramaiah, R.; Tsai, H.; Nie, W.; Blancon, J.-C.; Melkonyan, F.; Cao, D. H.; Traoré, B.; Pedesseau, L.; Kepenekian, M.; Katan, C.; Even, J.; Marks, T. J.; Navrotsky, A.; Mohite, A. D.; Stoumpos, C. C.; Kanatzidis, M. G. Structural and Thermodynamic Limits of Layer Thickness in 2D Halide Perovskites. *Proc. Natl. Acad. Sci. U. S. A.* **2019**, *116*, 58–66.

(16) Mao, L.; Kennard, R. M.; Traore, B.; Ke, W.; Katan, C.; Even, J.; Chabinyc, M. L.; Stoumpos, C. C.; Kanatzidis, M. G. Seven-Layered 2D Hybrid Lead Iodide Perovskites. *Chem* **2019**, *5*, 2593–2604.

(17) Paritmongkol, W.; Dahod, N. S.; Stollmann, A.; Mao, N.; Settens, C.; Zheng, S.-L.; Tisdale, W. A. Synthetic Variation and Structural Trends in Layered Two-Dimensional Alkylammonium Lead Halide Perovskites. *Chem. Mater.* **2019**, *31*, 5592–5607.

(18) Venkatesan, N. R.; Kennard, R. M.; DeCrescent, R. A.; Nakayama, H.; Dahlman, C. J.; Perry, E. E.; Schuller, J. A.; Chabinyc, M. L. Phase Intergrowth and Structural Defects in Organic Metal Halide Ruddlesden–Popper Thin Films. *Chem. Mater.* **2018**, *30*, 8615–8623.
(19) Venkatesan, N. R.; Labram, J. G.; Chabinyc, M. L. Charge-Carrier Dynamics and Crystalline Texture of Layered Ruddlesden–Popper Hybrid Lead Iodide Perovskite Thin Films. *ACS Energy Lett.* **2018**, *3*, 380–386.
(20) Dahlman, C. J.; DeCrescent, R. A.; Venkatesan, N. R.; Kennard, R. M.; Wu, G.; Everest, M. A.; Schuller, J. A.; Chabinyc, M. L. Controlling Solvate Intermediate Growth for Phase-Pure Organic Lead Iodide Ruddlesden–Popper $(C_4H_9NH_3)_2(CH_3NH_3)_{n-1}Pb_nI_{3n+1}$ Perovskite Thin Films. *Chem. Mater.* **2019**, *31*, 5832–5844.
(21) Proppe, A. H.; Quintero-Bermudez, R.; Tan, H.; Voznyy, O.; Kelley, S. O.; Sargent, E. H. Synthetic Control over Quantum Well Width Distribution and Carrier Migration in Low-Dimensional Perovskite Photovoltaics. *J. Am. Chem. Soc.* **2018**, *140*, 2890–2896.
(22) Zhang, X.; Munir, R.; Xu, Z.; Liu, Y.; Tsai, H.; Nie, W.; Li, J.; Niu, T.; Smilgies, D.-M.; Kanatzidis, M. G.; Mohite, A. D.; Zhao, K.; Amassian, A.; Liu, S. (Frank). Phase Transition Control for High Performance Ruddlesden–Popper Perovskite Solar Cells. *Adv. Mater.* **2018**, *30*, 1707166.
(23) Quintero-Bermudez, R.; Gold-Parker, A.; Proppe, A. H.; Munir, R.; Yang, Z.; Kelley, S. O.; Amassian, A.; Toney, M. F.; Sargent, E. H. Compositional and Orientational Control in Metal Halide Perovskites of Reduced Dimensionality. *Nat. Mater.* **2018**, *17*, 900.
(24) Zhou, N.; Shen, Y.; Li, L.; Tan, S.; Liu, N.; Zheng, G.; Chen, Q.; Zhou, H. Exploration of Crystallization Kinetics in Quasi Two-Dimensional Perovskite and High Performance Solar Cells. *J. Am. Chem. Soc.* **2018**, *140*, 459–465.
(25) Shamsi, J.; Urban, A. S.; Imran, M.; De Trizio, L.; Manna, L. Metal Halide Perovskite Nanocrystals: Synthesis, Post-Synthesis Modifications, and Their Optical Properties. *Chem. Rev.* **2019**, *119*, 3296–3348.
(26) Gonzalez-Carrero, S.; Francés-Soriano, L.; González-Béjar, M.; Agouram, S.; Galian, R. E.; Pérez-Prieto, J. The Luminescence of $CH_3NH_3PbBr_3$ Perovskite Nanoparticles Crests the Summit and Their Photostability under Wet Conditions Is Enhanced. *Small* **2016**, *12*, 5245–5250.
(27) Liu, F.; Zhang, Y.; Ding, C.; Kobayashi, S.; Izuishi, T.; Nakazawa, N.; Toyoda, T.; Ohta, T.; Hayase, S.; Minemoto, T.; Yoshino, K.; Dai, S.; Shen, Q. Highly Luminescent Phase-Stable $CsPbI_3$ Perovskite Quantum Dots Achieving Near 100% Absolute Photoluminescence Quantum Yield. *ACS Nano* **2017**, *11*, 10373–10383.
(28) Pan, J.; Shang, Y.; Yin, J.; De Bastiani, M.; Peng, W.; Dursun, I.; Sinatra, L.; El-Zohry, A. M.; Hedhili, M. N.; Emwas, A.-H.; Mohammed, O. F.; Ning, Z.; Bakr, O. M. Bidentate Ligand-Passivated $CsPbI_3$ Perovskite Nanocrystals for Stable Near-Unity Photoluminescence Quantum Yield and Efficient Red Light-Emitting Diodes. *J. Am. Chem. Soc.* **2018**, *140*, 562–565.
(29) Di Stasio, F.; Christodoulou, S.; Huo, N.; Konstantatos, G. Near-Unity Photoluminescence Quantum Yield in $CsPbBr_3$ Nanocrystal Solid-State Films *via* Postsynthesis Treatment with Lead Bromide. *Chem. Mater.* **2017**, *29*, 7663–7667.
(30) Protesescu, L.; Yakunin, S.; Bodnarchuk, M. I.; Krieg, F.; Caputo, R.; Hendon, C. H.; Yang, R. X.; Walsh, A.; Kovalenko, M. V. Nanocrystals of Cesium Lead Halide Perovskites ($CsPbX_3$, X = Cl, Br, and I): Novel Optoelectronic Materials Showing Bright Emission with Wide Color Gamut. *Nano Lett.* **2015**, *15*, 3692–3696.
(31) Swarnkar, A.; Marshall, A. R.; Sanehira, E. M.; Chernomordik, B. D.; Moore, D. T.; Christians, J. A.; Chakrabarti, T.; Luther, J. M. Quantum Dot–Induced Phase Stabilization of α-$CsPbI_3$ Perovskite for High-Efficiency Photovoltaics. *Science* **2016**, *354*, 92–95.
(32) Congreve, D. N.; Weidman, M. C.; Seitz, M.; Paritmongkol, W.; Dahod, N. S.; Tisdale, W. A. Tunable Light-Emitting Diodes Utilizing Quantum-Confined Layered Perovskite Emitters. *ACS Photonics* **2017**, *4*, 476–481.

(33) Yassitepe, E.; Yang, Z.; Voznyy, O.; Kim, Y.; Walters, G.; Castañeda, J. A.; Kanjanaboos, P.; Yuan, M.; Gong, X.; Fan, F.; Pan, J.; Hoogland, S.; Comin, R.; Bakr, O. M.; Padilha, L. A.; Nogueira, A. F.; Sargent, E. H. Amine-Free Synthesis of Cesium Lead Halide Perovskite Quantum Dots for Efficient Light-Emitting Diodes. *Adv. Funct. Mater.* **2016**, *26*, 8757–8763.
(34) Akkerman, Q. A.; Rainò, G.; Kovalenko, M. V.; Manna, L. Genesis, Challenges and Opportunities for Colloidal Lead Halide Perovskite Nanocrystals. *Nat. Mater.* **2018**, *17*, 394.
(35) Fu, Y.; Zhu, H.; Chen, J.; Hautzinger, M. P.; Zhu, X.-Y.; Jin, S. Metal Halide Perovskite Nanostructures for Optoelectronic Applications and the Study of Physical Properties. *Nat. Rev. Mater.* **2019**, *4*, 169.
(36) Moral, R. F.; Bonato, L. G.; Germino, J. C.; Coelho Oliveira, W. X.; Kamat, R.; Xu, J.; Tassone, C. J.; Stranks, S. D.; Toney, M. F.; Nogueira, A. F. Synthesis of Polycrystalline Ruddlesden–Popper Organic Lead Halides and Their Growth Dynamics. *Chem. Mater.* **2019**, *31*, 9472–9479.
(37) Dou, L.; Wong, A. B.; Yu, Y.; Lai, M.; Kornienko, N.; Eaton, S. W.; Fu, A.; Bischak, C. G.; Ma, J.; Ding, T.; Ginsberg, N. S.; Wang, L.-W.; Alivisatos, A. P.; Yang, P. Atomically Thin Two-Dimensional Organic-Inorganic Hybrid Perovskites. *Science* **2015**, *349*, 1518–1521.
(38) Ha, S. K.; Mauck, C. M.; Tisdale, W. A. Toward Stable Deep-Blue Luminescent Colloidal Lead Halide Perovskite Nanoplatelets: Systematic Photostability Investigation. *Chem. Mater.* **2019**, *31*, 2486–2496.
(39) Tong, Y.; Ehrat, F.; Vanderlinden, W.; Cardenas-Daw, C.; Stolarczyk, J. K.; Polavarapu, L.; Urban, A. S. Dilution-Induced Formation of Hybrid Perovskite Nanoplatelets. *ACS Nano* **2016**, *10*, 10936–10944.
(40) Cho, J.; Choi, Y.-H.; O'Loughlin, T. E.; De Jesus, L.; Banerjee, S. Ligand-Mediated Modulation of Layer Thicknesses of Perovskite Methylammonium Lead Bromide Nanoplatelets. *Chem. Mater.* **2016**, *28*, 6909–6916.
(41) Cho, J.; Jin, H.; Sellers, D. G.; Watson, D. F.; Son, D. H.; Banerjee, S. Influence of Ligand Shell Ordering on Dimensional Confinement of Cesium Lead Bromide ($CsPbBr_3$) Perovskite Nanoplatelets. *J. Mater. Chem. C* **2017**, *5*, 8810–8818.
(42) Cho, J.; Banerjee, S. Ligand-Directed Stabilization of Ternary Phases: Synthetic Control of Structural Dimensionality in Solution-Grown Cesium Lead Bromide Nanocrystals. *Chem. Mater.* **2018**, *30*, 6144–6155.
(43) Ahmed, G. H.; Yin, J.; Bose, R.; Sinatra, L.; Alarousu, E.; Yengel, E.; AlYami, N. M.; Saidaminov, M. I.; Zhang, Y.; Hedhili, M. N.; Bakr, O. M.; Brédas, J.-L.; Mohammed, O. F. Pyridine-Induced Dimensionality Change in Hybrid Perovskite Nanocrystals. *Chem. Mater.* **2017**, *29*, 4393–4400.
(44) Levchuk, I.; Osvet, A.; Tang, X.; Brandl, M.; Perea, J. D.; Hoegl, F.; Matt, G. J.; Hock, R.; Batentschuk, M.; Brabec, C. J. Brightly Luminescent and Color-Tunable Formamidinium Lead Halide Perovskite $FAPbX_3$ (X = Cl, Br, I) Colloidal Nanocrystals. *Nano Lett.* **2017**, *17*, 2765–2770.
(45) Sichert, J. A.; Tong, Y.; Mutz, N.; Vollmer, M.; Fischer, S.; Milowska, K. Z.; García Cortadella, R.; Nickel, B.; Cardenas-Daw, C.; Stolarczyk, J. K.; Urban, A. S.; Feldmann, J. Quantum Size Effect in Organometal Halide Perovskite Nanoplatelets. *Nano Lett.* **2015**, *15*, 6521–6527.
(46) Tyagi, P.; Arveson, S. M.; Tisdale, W. A. Colloidal Organohalide Perovskite Nanoplatelets Exhibiting Quantum Confinement. *J. Phys. Chem. Lett.* **2015**, *6*, 1911–1916.
(47) Bekenstein, Y.; Koscher, B. A.; Eaton, S. W.; Yang, P.; Alivisatos, A. P. Highly Luminescent Colloidal Nanoplates of Perovskite Cesium Lead Halide and Their Oriented Assemblies. *J. Am. Chem. Soc.* **2015**, *137*, 16008–16011.
(48) Weidman, M. C.; Goodman, A. J.; Tisdale, W. A. Colloidal Halide Perovskite Nanoplatelets: An Exciting New Class of Semiconductor Nanomaterials. *Chem. Mater.* **2017**, *29*, 5019–5030.
(49) Almeida, G.; Infante, I.; Manna, L. Resurfacing Halide Perovskite Nanocrystals. *Science* **2019**, *364*, 833–834.

(50) Nenon, D. P.; Pressler, K.; Kang, J.; Koscher, B. A.; Olshansky, J. H.; Osowiecki, W. T.; Koc, M. A.; Wang, L.-W.; Alivisatos, A. P. Design Principles for Trap-Free $CsPbX_3$ Nanocrystals: Enumerating and Eliminating Surface Halide Vacancies with Softer Lewis Bases. *J. Am. Chem. Soc.* **2018**, *140*, 17760–17772.
(51) Liu, Y.; Siron, M.; Lu, D.; Yang, J.; dos Reis, R.; Cui, F.; Gao, M.; Lai, M.; Lin, J.; Kong, Q.; Lei, T.; Kang, J.; Jin, J.; Ciston, J.; Yang, P. Self-Assembly of Two-Dimensional Perovskite Nanosheet Building Blocks into Ordered Ruddlesden–Popper Perovskite Phase. *J. Am. Chem. Soc.* **2019**, *141*, 13028–13032.
(52) Vybornyi, O.; Yakunin, S.; Kovalenko, M. V. Polar-Solvent-Free Colloidal Synthesis of Highly Luminescent Alkylammonium Lead Halide Perovskite Nanocrystals. *Nanoscale* **2016**, *8*, 6278–6283.
(53) Dang, Z.; Dhanabalan, B.; Castelli, A.; Dhall, R.; Bustillo, K. C.; Marchelli, D.; Spirito, D.; Petralanda, U.; Shamsi, J.; Manna, L.; Krahne, R.; Arciniegas, M. P. Temperature-Driven Transformation of $CsPbBr_3$ Nanoplatelets into Mosaic Nanotiles in Solution through Self-Assembly. *Nano Lett.* **2020**, *20*, 1808–1818.
(54) Zhang, D.; Yu, Y.; Bekenstein, Y.; Wong, A. B.; Alivisatos, A. P.; Yang, P. Ultrathin Colloidal Cesium Lead Halide Perovskite Nanowires. *J. Am. Chem. Soc.* **2016**, *138*, 13155–13158.
(55) Dong, Y.; Qiao, T.; Kim, D.; Parobek, D.; Rossi, D.; Son, D. H. Precise Control of Quantum Confinement in Cesium Lead Halide Perovskite Quantum Dots *via* Thermodynamic Equilibrium. *Nano Lett.* **2018**, *18*, 3716–3722.
(56) Imran, M.; Di Stasio, F.; Dang, Z.; Canale, C.; Khan, A. H.; Shamsi, J.; Brescia, R.; Prato, M.; Manna, L. Colloidal Synthesis of Strongly Fluorescent $CsPbBr_3$ Nanowires with Width Tunable down to the Quantum Confinement Regime. *Chem. Mater.* **2016**, *28*, 6450–6454.
(57) De Roo, J.; Ibáñez, M.; Geiregat, P.; Nedelcu, G.; Walravens, W.; Maes, J.; Martins, J. C.; Van Driessche, I.; Kovalenko, M. V.; Hens, Z. Highly Dynamic Ligand Binding and Light Absorption Coefficient of Cesium Lead Bromide Perovskite Nanocrystals. *ACS Nano* **2016**, *10*, 2071–2081.
(58) Tanaka, K.; Takahashi, T.; Ban, T.; Kondo, T.; Uchida, K.; Miura, N. Comparative Study on the Excitons in Lead-Halide-Based Perovskite-Type Crystals $CH_3NH_3PbBr_3$ $CH_3NH_3PbI_3$. *Solid State Commun.* **2003**, *127*, 619–623.
(59) Umemoto, K.; Takeda, M.; Tezuka, Y.; Chiba, T.; Schuette White, M.; Inose, T.; Yoshida, T.; Asakura, S.; Toyouchi, S.; Uji-i, H.; Masuhara, A. Separation of Mono-Dispersed $CH_3NH_3PbBr_3$ Perovskite Quantum Dots *via* Dissolution of Nanocrystals. *CrystEngComm* **2018**, *20*, 7053–7057.
(60) Ishihara, T.; Takahashi, J.; Goto, T. Optical Properties Due to Electronic Transitions in Two-Dimensional Semiconductors $(C_nH_{2n+1}NH_3)_2PbI_4$. *Phys. Rev. B* **1990**, *42*, 11099–11107.
(61) Keldysh, L. V. Coulomb Interaction in Thin Semiconductor and Semimetal Films. *Soviet J. Exper. Theor. Phys. Lett.* **1979**, *29*, 716–719.
(62) Muljarov, E. A.; Tikhodeev, S. G.; Gippius, N. A.; Ishihara, T. Excitons in Self-Organized Semiconductor/Insulator Superlattices: PbI-Based Perovskite Compounds. *Phys. Rev. B* **1995**, *51*, 14370–14378.
(63) Venkatesan, N. R.; Mahdi, A.; Barraza, B.; Wu, G.; Chabinyc, M. L.; Seshadri, R. Enhanced Yield-Mobility Products in Hybrid Halide Ruddlesden–Popper Compounds with Aromatic Ammonium Spacers. *Dalton Trans.* **2019**, *48*, 14019–14026.
(64) Tian, T.; Scullion, D.; Hughes, D.; Li, L. H.; Shih, C.-J.; Coleman, J.; Chhowalla, M.; Santos, E. J. G. Electronic Polarizability as the Fundamental Variable in the Dielectric Properties of Two-Dimensional Materials. *Nano Lett.* **2020**, *20*, 841–851.
(65) DeCrescent, R. A.; Venkatesan, N. R.; Dahlman, C. J.; Kennard, R. M.; Chabinyc, M. L.; Schuller, J. A. Optical Constants and Effective-Medium Origins of Large Optical Anisotropies in Layered Hybrid Organic/Inorganic Perovskites. *ACS Nano* **2019**, *13*, 10745–10753.
(66) Tanaka, K.; Takahashi, T.; Kondo, T.; Umebayashi, T.; Asai, K.; Ema, K. Image Charge Effect on Two-Dimensional Excitons in an Inorganic-Organic Quantum-Well Crystal. *Phys. Rev. B* **2005**, *71*, 045312.

(67) Boles, M. A.; Ling, D.; Hyeon, T.; Talapin, D. V. The Surface Science of Nanocrystals. *Nat. Mater.* **2016**, *15*, 141–153.
(68) Weidman, M. C.; Seitz, M.; Stranks, S. D.; Tisdale, W. A. Highly Tunable Colloidal Perovskite Nanoplatelets through Variable Cation, Metal, and Halide Composition. *ACS Nano* **2016**, *10*, 7830–7839.
(69) Krieg, F.; Ochsenbein, S. T.; Yakunin, S.; ten Brinck, S.; Aellen, P.; Süess, A.; Clerc, B.; Guggisberg, D.; Nazarenko, O.; Shynkarenko, Y.; Kumar, S.; Shih, C.-J.; Infante, I.; Kovalenko, M. V. Colloidal $CsPbX_3$ (X = Cl, Br, I) Nanocrystals 2.0: Zwitterionic Capping Ligands for Improved Durability and Stability. *ACS Energy Lett.* **2018**, *3*, 641–646.
(70) Dahod, N. S.; Paritmongkol, W.; Stollmann, A.; Settens, C.; Zheng, S.-L.; Tisdale, W. A. Melting Transitions of the Organic Subphase in Layered Two-Dimensional Halide Perovskites. *J. Phys. Chem. Lett.* **2019**, *10*, 2924–2930.
(71) Sichert, J. A.; Hemmerling, A.; Cardenas-Daw, C.; Urban, A. S.; Feldmann, J. Tuning the Optical Bandgap in Layered Hybrid Perovskites through Variation of Alkyl Chain Length. *APL Materials* **2019**, *7*, 041116.
(72) Billing, D. G.; Lemmerer, A. Synthesis, Characterization and Phase Transitions of the Inorganic–Organic Layered Perovskite-Type Hybrids $[(C_nH_{2n+1}NH_3)_2PbI_4]$ (n = 12, 14, 16 and 18). *New J. Chem.* **2008**, *32*, 1736–1746.
(73) Billing, D. G.; Lemmerer, A. Synthesis, Characterization and Phase Transitions in the Inorganic–Organic Layered Perovskite-Type Hybrids $[(C_nH_{2n+1}NH_3)_2PbI_4]$, n = 4, 5 and 6. *Acta Crystallogr. Sect. B* **2007**, *63*, 735–747.
(74) Venkataraman, N. V.; Bhagyalakshmi, S.; Vasudevan, S.; Seshadri, R. Conformation and Orientation of Alkyl Chains in the Layered Organic–Inorganic Hybrids: $(C_nH_{2n+1}NH_3)_2PbI_4$ (n = 12,16,18). *Phys. Chem. Chem. Phys.* **2002**, *4*, 4533–4538.
(75) Lemmerer, A.; Billing, D. G. Synthesis, Characterization and Phase Transitions of the Inorganic–Organic Layered Perovskite-Type Hybrids $[(C_nH_{2n+1}NH_3)_2PbI_4]$, n = 7, 8, 9 and 10. *Dalton Trans.* **2012**, *41*, 1146–1157.
(76) Jana, S.; Phan, T. N. T.; Bouet, C.; Tessier, M. D.; Davidson, P.; Dubertret, B.; Abécassis, B. Stacking and Colloidal Stability of CdSe Nanoplatelets. *Langmuir* **2015**, *31*, 10532–10539.
(77) Tanford, C. Micelle Shape and Size. *J. Phys. Chem.* **1972**, *76*, 3020–3024.
(78) Blancon, J.-C.; Tsai, H.; Nie, W.; Stoumpos, C. C.; Pedesseau, L.; Katan, C.; Kepenekian, M.; Soe, C. M. M.; Appavoo, K.; Sfeir, M. Y.; Tretiak, S.; Ajayan, P. M.; Kanatzidis, M. G.; Even, J.; Crochet, J. J.; Mohite, A. D. Extremely Efficient Internal Exciton Dissociation through Edge States in Layered 2D Perovskites. *Science* **2017**, *355*, 1288–1292.
(79) Bala, A.; Kumar, V. Role of Ligand-Ligand Interactions in the Stabilization of Thin Layers of Tin Bromide Perovskite: An *Ab Initio* Study of the Atomic and Electronic Structure, and Optical Properties. *J. Phys. Chem. C* **2019**, *123*, 25176–25184.
(80) Kister, T.; Monego, D.; Mulvaney, P.; Widmer-Cooper, A.; Kraus, T. Colloidal Stability of Apolar Nanoparticles: The Role of Particle Size and Ligand Shell Structure. *ACS Nano* **2018**, *12*, 5969–5977.
(81) Lira-Galeana, C.; Firoozabadi, A.; Prausnitz, J. M. Thermodynamics of Wax Precipitation in Petroleum Mixtures. *AIChE J.* **1996**, *42*, 239–248.
(82) Wei, Y.; Chu, H.; Tian, Y.; Chen, B.; Wu, K.; Wang, J.; Yang, X.; Cai, B.; Zhang, Y.; Zhao, J. Reverse-Graded 2D Ruddlesden–Popper Perovskites for Efficient Air-Stable Solar Cells. *Adv. Energy Mater.* **2019**, *9*, 1900612.
(83) Pakes, P. W.; Rounds, T. C.; Strauss, H. L. Conformations of Cyclooctane and Some Related Oxocanes. *J. Phys. Chem.* **1981**, *85*, 2469–2475.
(84) Naik, V. V.; Vasudevan, S. Effect of Alkyl Chain Arrangement on Conformation and Dynamics in a Surfactant Intercalated Layered Double Hydroxide: Spectroscopic Measurements and MD Simulations. *J. Phys. Chem. C* **2011**, *115*, 8221–8232.

(85) Manser, J. S.; Saidaminov, M. I.; Christians, J. A.; Bakr, O. M.; Kamat, P. V. Making and Breaking of Lead Halide Perovskites. *Acc. Chem. Res.* **2016**, *49*, 330–338.
(86) Blancon, J.-C.; Stier, A. V.; Tsai, H.; Nie, W.; Stoumpos, C. C.; Traoré, B.; Pedesseau, L.; Kepenekian, M.; Katsutani, F.; Noe, G. T.; Kono, J.; Tretiak, S.; Crooker, S. A.; Katan, C.; Kanatzidis, M. G.; Crochet, J. J.; Even, J.; Mohite, A. D. Scaling Law for Excitons in 2D Perovskite Quantum Wells. *Nat. Commun.* **2018**, *9*, 2254.
(87) Bertolotti, F.; Nedelcu, G.; Vivani, A.; Cervellino, A.; Masciocchi, N.; Guagliardi, A.; Kovalenko, M. V. Crystal Structure, Morphology, and Surface Termination of Cyan-Emissive, Six-Monolayers-Thick $CsPbBr_3$ Nanoplatelets from X-Ray Total Scattering. *ACS Nano* **2019**, *13*, 14294–14307.
(88) Wang, R.; Tong, Y.; Manzi, A.; Wang, K.; Fu, Z.; Kentzinger, E.; Feldmann, J.; Urban, A. S.; Müller-Buschbaum, P.; Frielinghaus, H. Preferential Orientation of Crystals Induced by Incorporation of Organic Ligands in Mixed-Dimensional Hybrid Perovskite Films. *Adv. Opt. Mater.* **2018**, *6*, 1701311.
(89) Teixeira, J. Small-Angle Scattering by Fractal Systems. *J. Appl. Cryst.* **1988**, *21*, 781–785.
(90) Leung, T. L.; Tam, H. W.; Liu, F.; Lin, J.; Ng, A. M. C.; Chan, W. K.; Chen, W.; He, Z.; Lončarić, I.; Grisanti, L.; Ma, C.; Wong, K. S.; Lau, Y. S.; Zhu, F.; Skoko, Ž.; Popović, J.; Djurišić, A. B. Mixed Spacer Cation Stabilization of Blue-Emitting n = 2 Ruddlesden–Popper Organic–Inorganic Halide Perovskite Films. *Adv. Opt. Mater.* **2019**, *8*, 1901679.
(91) Xu, Z.; Mitzi, D. B. SnI_4^{2-}-Based Hybrid Perovskites Templated by Multiple Organic Cations: Combining Organic Functionalities through Noncovalent Interactions. *Chem. Mater.* **2003**, *15*, 3632–3637.
(92) Ho, D. L.; Briber, R. M.; Glinka, C. J. Characterization of Organically Modified Clays Using Scattering and Microscopy Techniques. *Chem. Mater.* **2001**, *13*, 1923–1931.
(93) Ha, S. K.; Tisdale, W. A. Facile Synthesis of Colloidal Lead Halide Perovskite Nanoplatelets *via* Ligand-Assisted Reprecipitation. *J. Visualized Exp.* **2019**, No. 152, e60114.
(94) Ilavsky, J. Nika: Software for Two-Dimensional Data Reduction. *J. Appl. Crystallogr.* **2012**, *45*, 324–328.
(95) Oosterhout, S. D.; Savikhin, V.; Zhang, J.; Zhang, Y.; Burgers, M. A.; Marder, S. R.; Bazan, G. C.; Toney, M. F. Mixing Behavior in Small Molecule:Fullerene Organic Photovoltaics. *Chem. Mater.* **2017**, *29*, 3062–3069.
(96) Kline, S. R. Reduction and Analysis of SANS and USANS Data Using IGOR Pro. *J. Appl. Cryst.* **2006**, *39*, 895–900.

Supporting Information

Structural Evolution of Layered Hybrid Lead Iodide Perovskites in Colloidal Dispersions

Clayton J. Dahlman,[†] Naveen R. Venkatesan,[†] Patrick T. Corona,[‡] Rhys M. Kennard,[†] Lingling Mao,[†] Noah C. Smith,[‡] Jiamin Zhang,[‡] Ram Seshadri,[†,+] Matthew E. Helgeson,[‡] Michael L. Chabinyc[†,*]

[†] Materials Department, University of California, Santa Barbara, California 93106, United States

[‡] Department of Chemical Engineering, University of California, Santa Barbara, California 93106, United States

[+]Department of Chemistry and Biochemistry, University of California, Santa Barbara, California 93106, United States

*Corresponding Author: mchabinyc@engineering.ucsb.edu

Contents

Defining the stoichiometry of colloidal samples

The stoichiometry of precursors during antisolvent precipitation of colloids was defined by the nominal *n*-value and the stoichiometry of mixed spacer compositions. For samples prepared with 'added' mixed spacers, the spacer *R* (*e.g.* cOEA or C12) was added to a nominal $n = 2$ stoichiometry of $C4_2MAPb_2I_7$. For samples prepared with 'substitutional' mixed spacers, the spacer *R* was substituted for C4 to retain the $n = 2$ stoichiometry. **Figure S1** illustrates how 'added' or 'substitutional' mixed spacer stoichiometries affect the total concentration of precursors in the mixture. Different *n* values for R-P compositions that only have C4 spacers are also shown for reference.

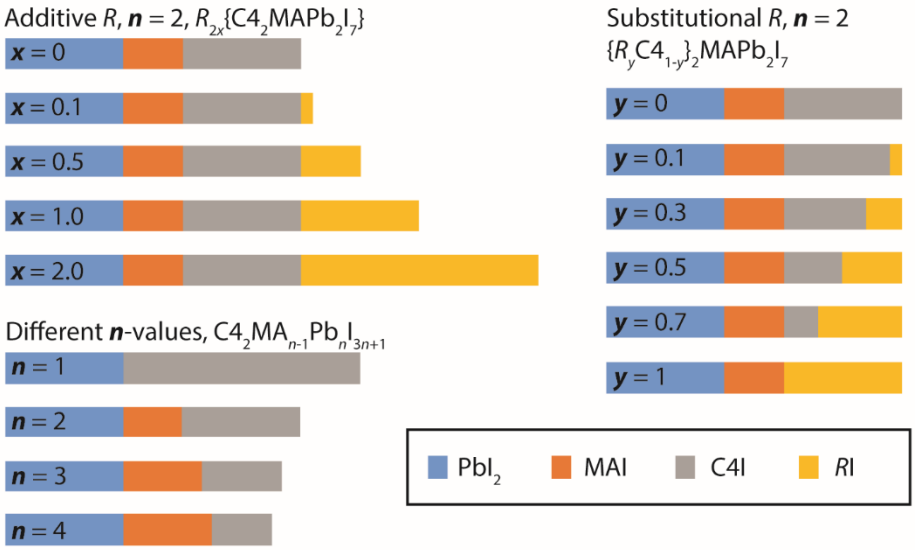

Figure S1. A schematic illustrating the precursor stoichiometries used to prepare colloidal layered lead iodide perovskite samples. The area of each bar is proportional to the molar quantity of precursor chemical (PbI_2, MAI, BAI, and *R*I where *R* is either C12 or cOEA) added during antisolvent precipitation of colloids. The quantity of PbI_2 is held constant in the illustration to reflect the consistent [Pb] = 0.5 M of each sample presented in the manuscript (unless otherwise noted).

Layered structure of Ruddlesden-Popper phases with different spacers

Approximating interlayer spacing from unit cell dimensions.

The interlayer separation was calculated from X-ray diffraction (XRD) measurements by assuming a Ruddlesden-Popper (R-P) unit cell. As described in the text, (0*k*0) reflections are distinguishable for $q < 1.0$ Å^{-1} and provide an estimate of the *b*-parameter. However, the *a* and *c* parameters of the unit cell cannot be reliably calculated from the polyphasic XRD patterns. The lead iodide octahedral height was approximated from *a* and *c* parameters reported for centrosymmetric structures of $C4_2MA_{n-1}Pb_nI_{3n+1}$.[1] The interlayer separation between lead iodide octahedral surfaces can then be estimated by subtracting the approximate octahedral heights from the measured *b* parameter, and assuming that the spacers partially insert between octahedral vertices (**Figure S2a**). Similarly, the areal packing of spacers across the lead iodide surface can be approximated based on the *a* and *c* parameters of the unit cell, because each octahedral site has a charge of -1 at the surface (**Figure S2b**). We note that these approximations do not account for octahedral tilting or distortions.

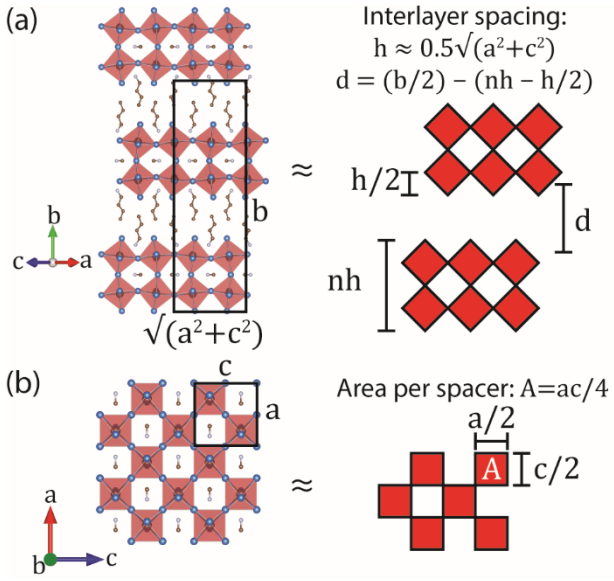

Figure S2. An illustration of the geometric approximations used to calculate the a) interlayer separation and b) area per spacer molecule of a R-P crystal with a tetragonal unit cell and particular *n*-value.

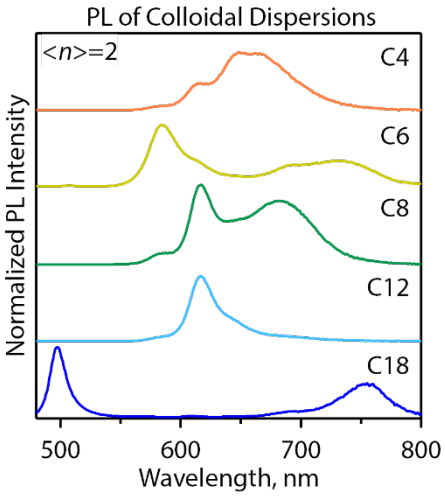

Figure S3. Photoluminescence spectra of dispersions of colloidal perovskites in toluene (~ 0.1 mmol Pb/L), prepared with an average precursor stoichiometry of <*n*> = 2 (*i.e.* $R_2MAPb_2I_7$) for linear alkylammonium spacers consistent with dropcast colloids measured by XRD in **Figure 3a**. The feature at 498 nm is observed for *n* = 1 R-Ps with long alkylammonium spacers (C12, C16, C18) because of octahedral tilting at room temperature, and is expected for *n* = 1 C18 R-Ps observed by XRD.[72]

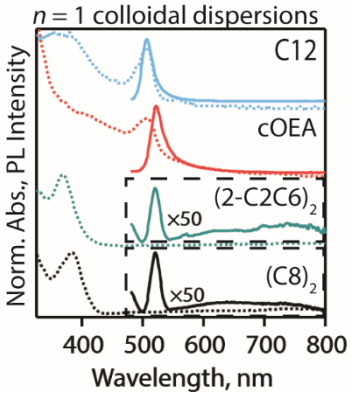

Figure S4. PL (solid lines) and absorbance (dashed lines) measurements of dispersions prepared from antisolvent precipitation of *n* = 1 lead halide R-P phases with different spacers, as shown in **Figure 4c**. PL spectra were obtained by excitation with 450 nm light. The PL for $(2\text{-}C2C6)_2$ and $(C8)_2$ spacers is magnified by 50× to reveal very weak PL features around 520 nm.

X-ray diffraction of colloidal dispersions

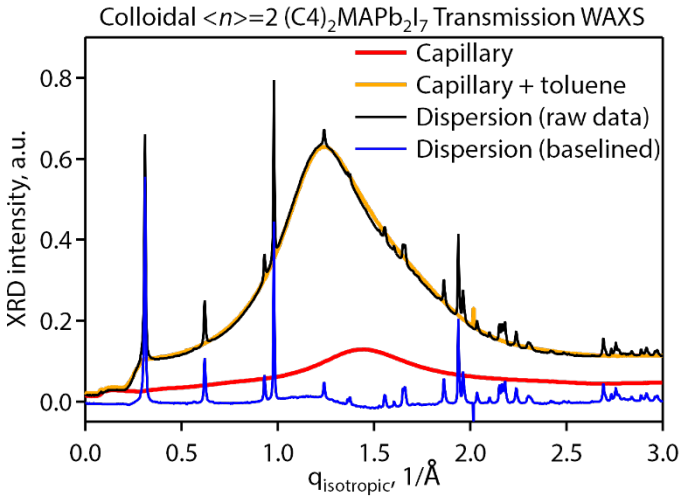

Figure S5. Transmission wide-angle X-ray scattering (WAXS) measurements for a dispersion of $\langle n \rangle = 2$ $(C4)_2MAPb_2I_7$ colloidal perovskites in toluene (black), calculated as isotropic averages of 2D transmission diffraction patterns. WAXS for an empty capillary is shown in red, and WAXS of a capillary filled with toluene is shown in orange normalized to the diffuse scattering profile of the colloidal perovskite scattering pattern. The diffraction pattern of the colloidal perovskites is obtained by subtracting the normalized capillary and toluene pattern from the raw transmission WAXS data, yielding the baselined pattern shown in blue.

Transmission WAXS measurements were performed on 2D perovskite dispersions to measure colloidal structure and to determine if solvent incorporates in the colloidal particles. Transmission WAXS of $n = 1$ colloidal dispersions prepared with only C4, C12 or cOEA spacers are compared to powder patterns of deposited films or single crystals in **Figure S6**. Single crystals of $n = 1$ cOEA R-Ps were too small for single crystal XRD, so a powder XRD measurement is shown instead. The excellent agreement between the *d*-spacings of colloidal R-P phases and single crystals reveals that solvent does not incorporate in the colloidal R-Ps. Moreover, the peak intensities of transmission WAXS of dispersions match simulated powder patterns. Thus, $n = 1$ colloids prepared by antisolvent precipitation are structurally identical to 2D R-P phases, but with small grain sizes and stabilizing surface ligands that enable dispersion in non-polar solvent.

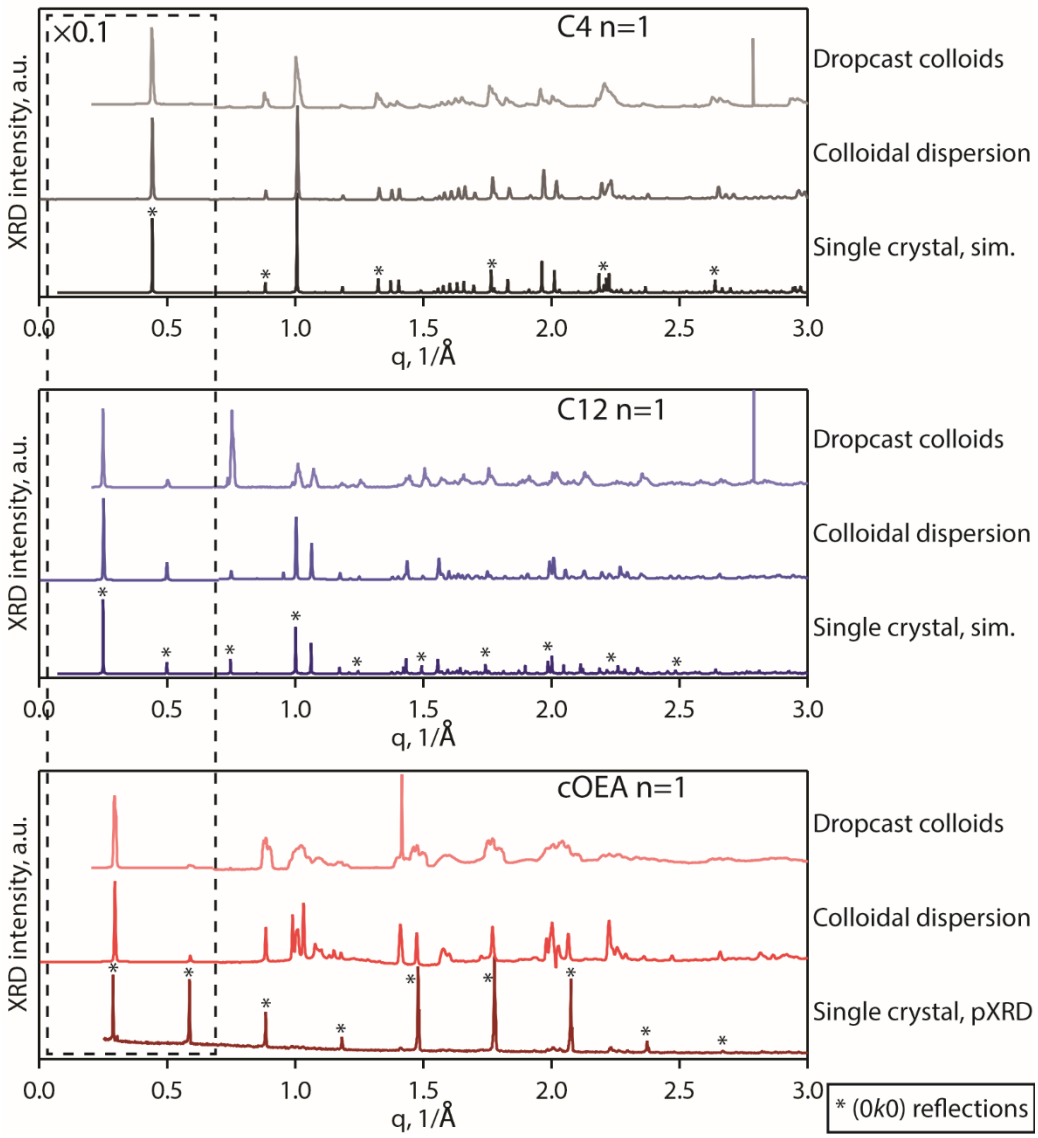

Figure S6. X-ray diffraction (XRD) patterns obtained by different methods for n = 1 phases of $C4_2PbI_4$, $C12_2PbI_4$ and $cOEA_2PbI_4$. XRD is compared between transmission WAXS of dispersed colloidal perovskites (lightest color), grazing-incidence wide-angle X-ray scattering (GIWAXS) of drop-cast colloidal perovskites shown as isotropic averages across q (intermediate color), and XRD of single crystals of each phase (darkest color). The single crystal patterns for C4 and C12 spacers were simulated from reported crystal structures.[1,2] The single crystal pattern for $cOEA_2PbI_4$ was measured from a powder because the structure has not been reported in the literature and the crystallites were too small for single-crystal diffraction measurements. The peaks marked by an asterisk (*) in the single crystal patterns correspond to (0k0) reflections. Peak intensities in the low q region bounded by the dashed line were reduced by a factor of 0.1 to magnify diffraction from reflections at higher q.

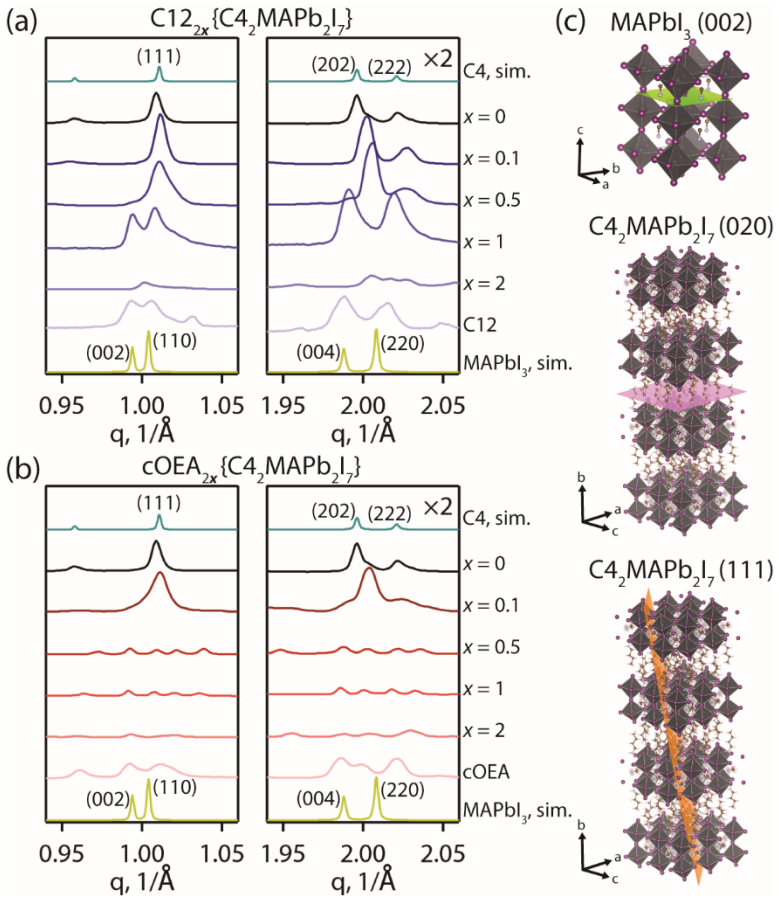

Figure S7. Expanded regions of the transmission wide-angle X-ray scattering obtained through 10 mmol Pb/L colloidal dispersions in toluene prepared with C4-spacers, $MAPbI_x$ perovskite precursors and either (a) C12 or (b) cOEA ligands, as shown in **Figure 6**. Spacer cations were added to an $\langle n \rangle = 2$ precursor mixture of $C4_2MAPb_2I_7$ prior to antisolvent preciptiation for an effective stoichiometry of either (a) $C12_{2x}\{C4_2MAPb_2I_7\}$ or (b) $cOEA_{2x}\{C4_2MAPb_2I_7\}$. Sections of the diffraction pattern are shown highlighting the (a) (111) or (b) (222) reflections expected for an $n = 2$ R-P crystal, as indicated in the unit cell schematics in (c). The intensities in the right panels are magnified 2× to resolve features at higher q. The simulated powder diffraction patterns are shown for centrosymmetric $n = 2$ $C4_2MAPb_2I_7$ ('C4, sim.', *Ccmm*)[1] and the room-temperature β phase of $CH_3NH_3PbI_3$ ('$MAPbI_3$, sim.', *I*4*cm*)[3].

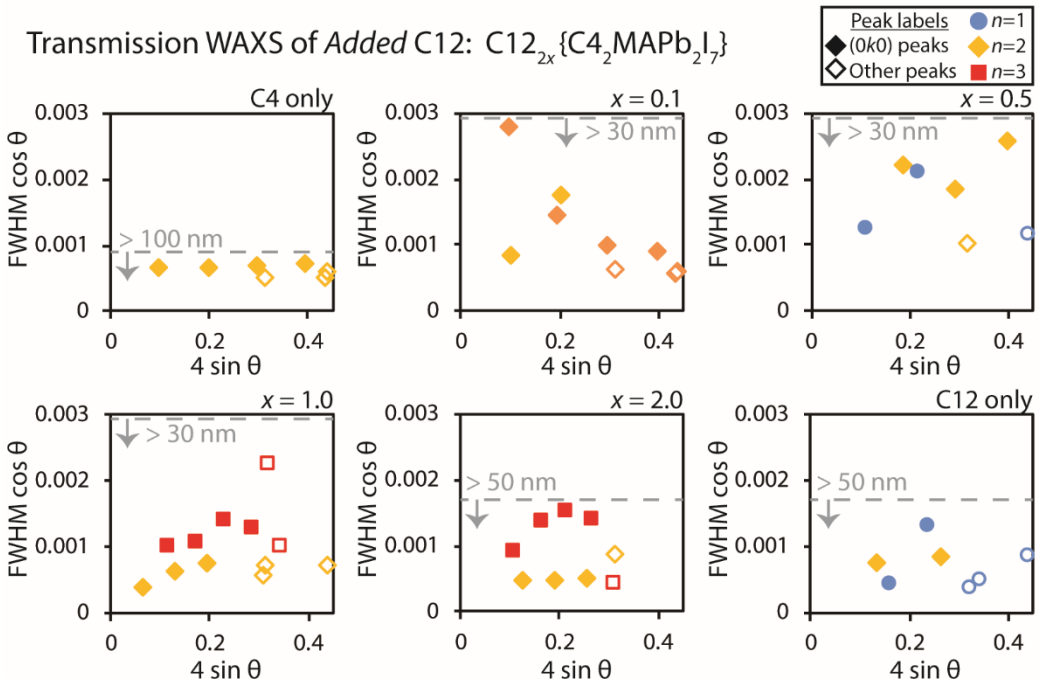

Figure S8. Williamson-Hall plots obtained from transmission wide-angle X-ray scattering through 10 mmol Pb/L colloidal dispersions in toluene. C4 spacers, $MAPbI_x$ perovskite precursors and C12 ligands were added to an $\langle n \rangle = 2$ precursor mixture of $C4_2MAPb_2I_7$ prior to antisolvent precipitation for an effective stoichiometry of $C12_{2x}\{C4_2MAPb_2I_7\}$, as shown in **Figure 6**. 'FWHM' is the full-width-half-maximum of the fitted Voigt peak for each reflection, measured in units of 2θ (radians), and θ is the Bragg angle. Instrumental broadening was found to be negligibly small within the uncertainty of peak fitting during these measurements. The filled-in markers indicate (0*k*0) reflections indexed to distinct R-P crystal phases, and the open markers indicate all other observed reflections. Grain sizes were estimated from the Scherrer broadening equation by assuming negligible strain broadening and taking the average of the indexed R-P (0*k*0) values of FWHM cos θ. The gray dashed lines indicate lower bounds on grain sizes for each sample.

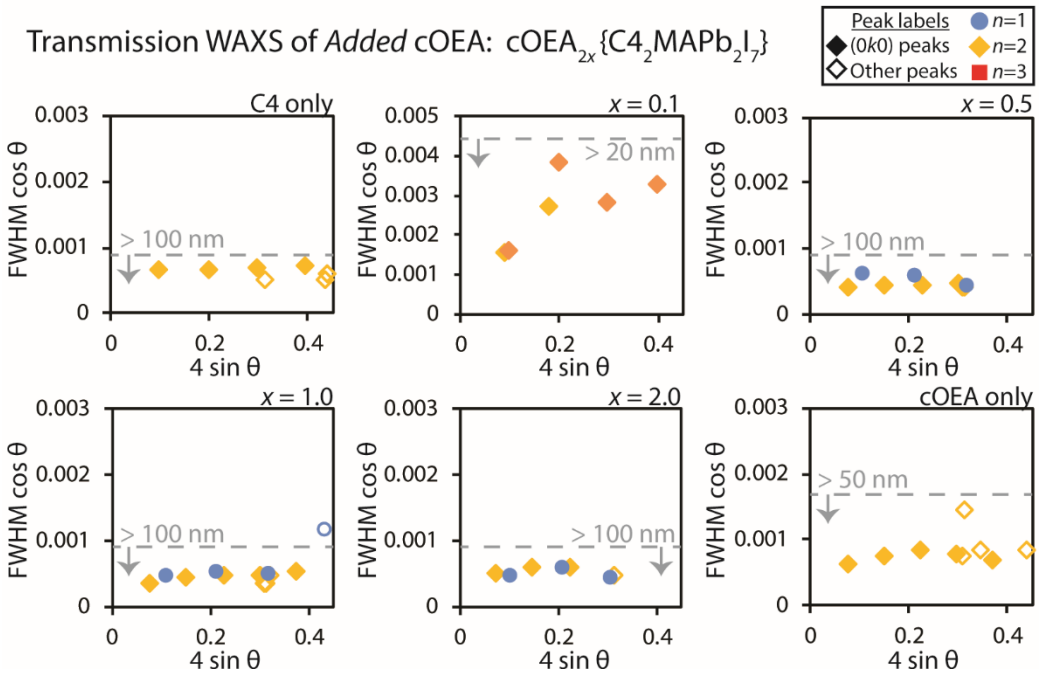

Figure S9. Williamson-Hall plots obtained from transmission wide-angle X-ray scattering through 10 mmol Pb/L colloidal dispersions in toluene. C4 spacers, $MAPbI_x$ perovskite precursors and cOEA ligands were added to an $\langle n \rangle = 2$ precursor mixture of $C4_2MAPb_2I_7$ prior to antisolvent precipitation for an effective stoichiometry of $cOEA_{2x}\{C4_2MAPb_2I_7\}$, as shown in **Figure 6**. 'FWHM' is the full-width-half-maximum of the fitted Voigt peak for each reflection, measured in units of 2θ (radians), and θ is the Bragg angle. Instrumental broadening was found to be negligibly small within the uncertainty of peak fitting during these measurements. The filled-in markers indicate (0*k*0) reflections indexed to distinct R-P crystal phases, and the open markers indicate all other observed reflections. Grain sizes were estimated from the Scherrer broadening equation by assuming negligible strain broadening and taking the average of the indexed R-P (0*k*0) values of FWHM cos θ. The gray dashed lines indicate lower bounds on grain sizes for each sample.

R-P crystallite grain sizes (**Table S1**) were estimated from transmission WAXS data shown in the Williamson-Hall plots of **Figure S8** and **S9**. Only the (0*k*0) reflections were used to estimate grain size, so the only estimated grain dimension is the particle 'height' (*i.e.* number of layers, **Figure 2**) along the <0*k*0> direction. The grain size was measured by:

$$\text{Particle 'height'} = \frac{K\lambda}{\text{FWHM}\cos\theta}$$

Here, K is the Scherrer constant ($K = 0.9$ for all calculations), λ is the beam wavelength ($\lambda = 0.9763$ Å), 'FWHM' is the full-width-half-maximum of the fitted Voigt peak for each reflection, measured in units of 2θ (radians), and θ is the Bragg angle.

Table S1. Grain sizes estimated from transmission WAXS measurements of $\langle n \rangle = 2$ $(R)_{2x}\{BA_2MAPb_2I_7\}$ compositions of perovskite colloids prepared with added C12 or cOEA. The interlayer distance and grain sizes calculated from WAXS measurements are matched to the indexed phases indicated by the colored markers and simulated reflections shown in **Figure 6**.

$\{R_2\}_x\{C4_2MAPb_2I_7\}$	Phase	Interlayer *d*, Å	(0*k*0) $D_{scherrer}$, Å
cOEA **only**	◆ ***n*=2**	**16.8 ± 0.1**	**> 1212 ± 124**
cOEA ***x* = 1.0**	◆ ***n*=2**	**16.7 ± 0.05**	**> 1904 ± 245**
	○ *n*=1	15.5 ± 0.02	> 1727 ± 101
cOEA ***x* = 0.1**	◆ ***n*=2**	**12.5 ± 0.1**	**> 405 ± 153**
	◇ *n*=2	10.5 ± 0.4	> 303 ± 99
C12 **only**	● ***n*=1**	**21.5 ± 0.2**	**> 1065 ± 579**
	◇ *n*=2	20.3 ± 0.01	> 1090 ± 100
C12 ***x* = 1.0**	◆ ***n*=2**	**20.8 ± 0.2**	**> 1949 ± 1427**
	□ *n*=3	18.8 ± 0.1	> 724 ± 109
C12 ***x* = 0.1**	◆ ***n*=2**	**10.0 ± 0.1**	**> 590 ± 224**
	◇ *n*=2	10.5 ± 0.3	> 578 ± 289
C4 **only**	◆ ***n*=2**	**10.3 ± 0.04**	**> 1243 ± 140**

Mixed spacer compositions with fixed cation stoichiometry

The stoichiometry of perovskite colloids prepared with mixed spacers, *e.g.* C4 and C12 or C4 and cOEA, can be defined by either adding excess C12 or cOEA to $C4_2MA_{n-1}Pb_nI_{3n+1}$ or by substituting C12 or cOEA for C4 for a consistent $(RNH_3)_2MA_{n-1}Pb_nI_{3n+1}$. The manuscript highlights the case where excess C12 or cOEA are added, but optical and diffraction measurements of precursor stoichiometries with substitutional C12 or cOEA are provided below.

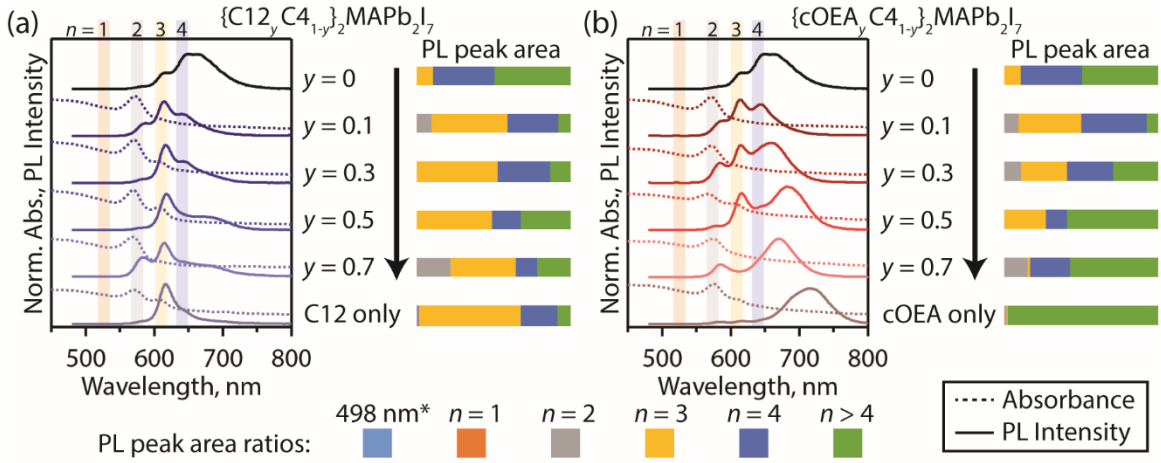

Figure S10. Normalized PL spectra (solid lines) and absorbance spectra (dashed lines) of ~ 0.1 mmol Pb/L colloidal dispersions in toluene prepared with C4, $MAPbI_x$ perovskite precursors and either (a) C12 or (b) cOEA ligands. PL spectra were obtained by excitation with 450 nm light. Spacer cations were substituted for C4 in $\langle n \rangle = 2$ precursor solutions prior to antisolvent precipitation for effective stoichiometries of either a) $\{C12_yBA_{1-y}\}_2MAPb_2I_7$ or b) $\{cOEA_yBA_{1-y}\}_2MAPb_2I_7$. The arrows indicate greater content of substituted C12 or cOEA species in the precursors. The bar graphs at the right of each plot indicate the fitted Lorentzian peak areas of for emission from different *n*-values. A peak at 498 nm (marked with *) is observed in distorted 2D phases of $C12_2PbI_4$.[4]

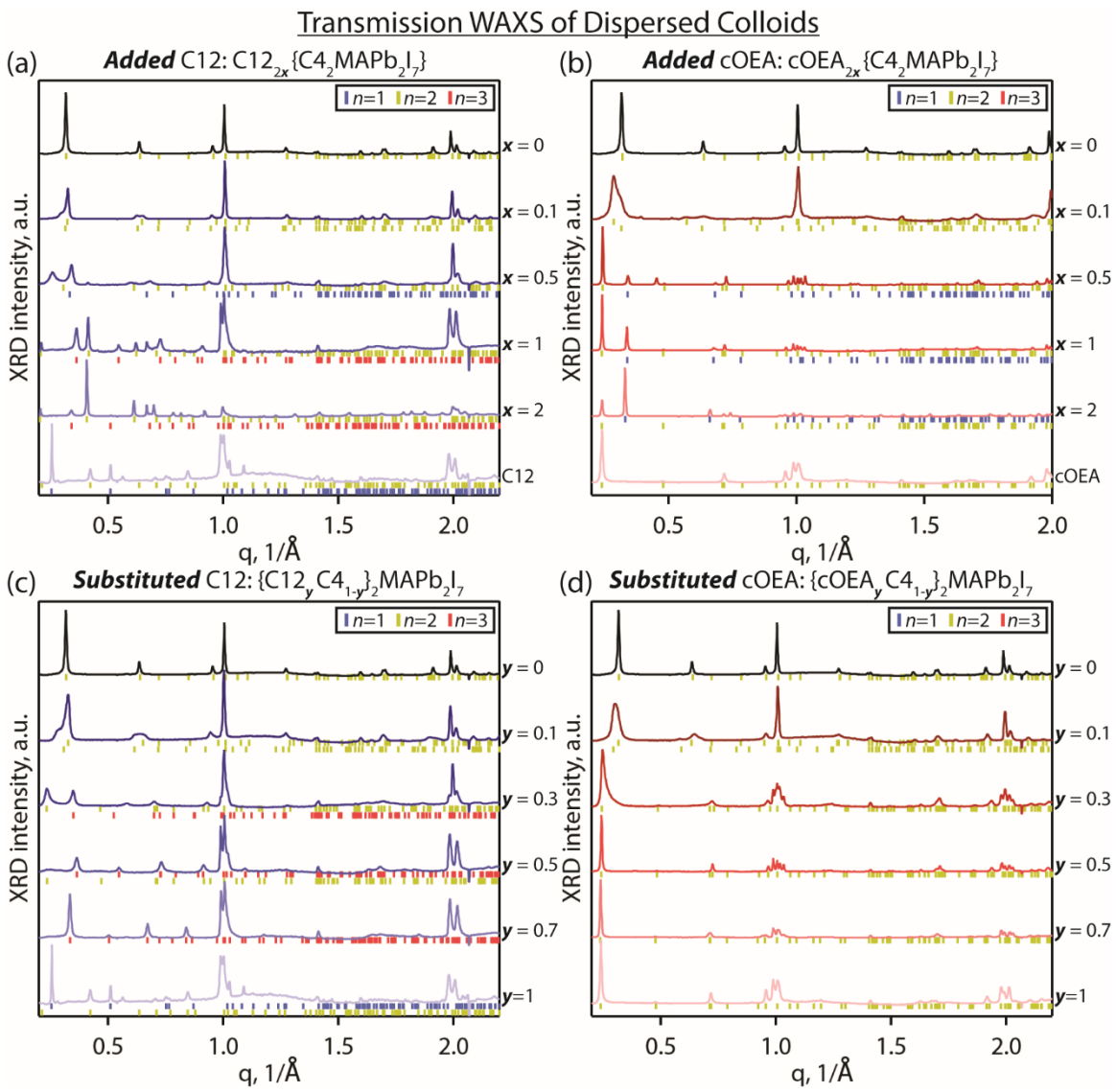

Figure S11. Transmission wide-angle X-ray scattering obtained through ~ 10 mmol Pb/L colloidal dispersions in toluene prepared with C4, $MAPbI_x$ perovskite precursors and either (a,c) C12 or (b,d) cOEA ligands. In the upper panels, spacer cations were added to an $\langle n \rangle = 2$ precursor mixture of $C4_2MAPb_2I_7$ prior to antisolvent precipitation for an effective stoichiometry of either a) $C12_{2x}\{C4_2MAPb_2I_7\}$ or b) $cOEA_{2x}\{C4_2MAPb_2I_7\}$, consistent with the measurements shown in **Figure 6**. In the lower panels, spacer cations were substituted for C4 in $\langle n \rangle = 2$ precursor solutions prior to antisolvent precipitation for effective stoichiometries of either c) $\{C12_yBA_{1-y}\}_2MAPb_2I_7$ or d) $\{cOEA_yBA_{1-y}\}_2MAPb_2I_7$. Simulated reflections for the two most dominant phases are shown underneath each measurement corresponding to n = 1,2 or 3 R-P phases with unit cell b parameters adjusted to fit the (0k0) peaks.

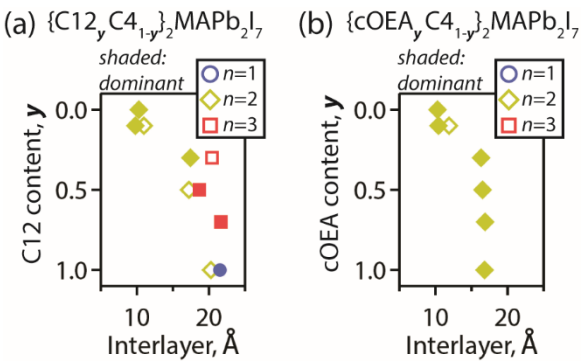

Figure S12. Estimated interlayer spacings for each of the transmission wide-angle X-ray scattering measurements shown in **Figure S11c,d** based on assignments of *n*-value and *b* parameters extracted from (0*k*0) reflections for each distinct phase. Colloids were prepared in toluene (~ 10 mmol Pb/L) with effective stoichiometries of either a) $\{C12_yC4_{1-y}\}_2MAPb_2I_7$ or b) $\{cOEA_yC4_{1-y}\}MAPb_2I_7$.

Comparing properties of colloidal dispersions and films

Added C12 or cOEA ligands to <*n*> = 2 $C4_2MAPb_2I_7$

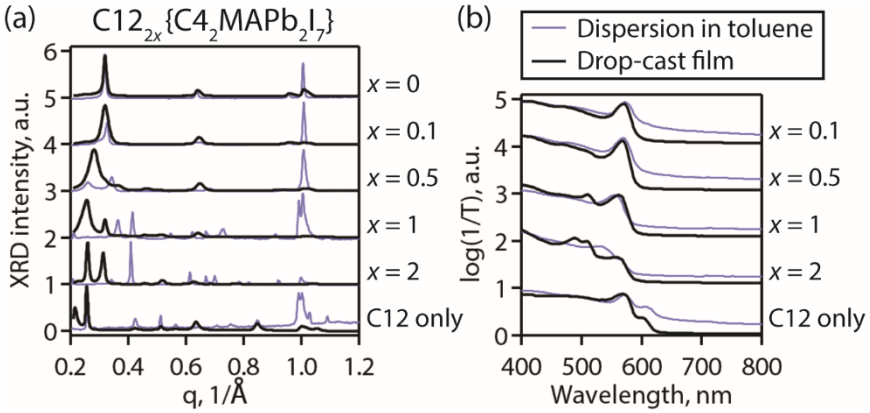

Figure S13. a) Wide-angle X-ray scattering (WAXS) and b) transmittance measurements of either colloidal dispersions in toluene (light blue lines) or drop-cast films of the same dispersions on quartz (black lines), for perovskite colloids prepared with C4, $MAPbI_x$ perovskite precursors and C12 ligands. C12 was added to an <*n*> = 2 precursor mixture of $C4_2MAPb_2I_7$ prior to antisolvent precipitation for an effective stoichiometry of $C12_{2x}\{C4_2MAPb_2I_7\}$. Transmission WAXS (a) was measured for ~ 10 mmol Pb/L dispersions in toluene, whereas optical transmittance (b) was measured for ~ 0.1 mmol Pb/L dispersions in toluene. Grazing-incidence WAXS, at an incidence angle of 0.1 degrees, was measured for drop-cast films in (a), and normal-incidence transmittance was measured for drop-cast films in (b), of approximately the same thickness. All WAXS and transmittance data were normalized by intensity.

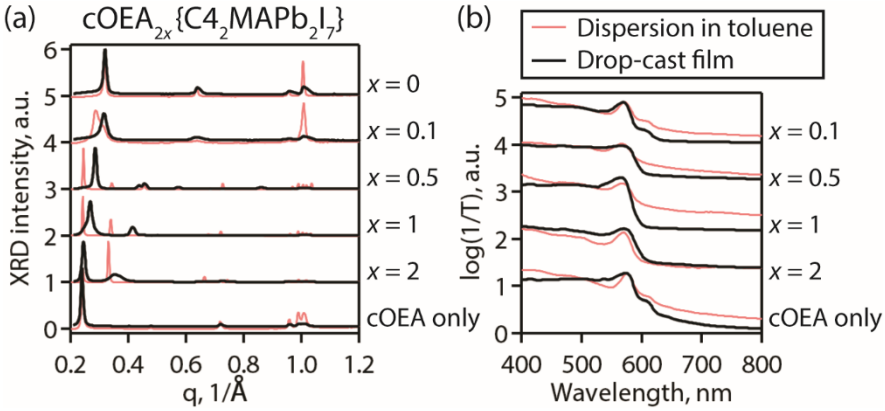

Figure S14. a) Wide-angle X-ray scattering (WAXS) and b) transmittance measurements of either colloidal dispersions in toluene (light red lines) or drop-cast films of the same dispersions on quartz (black lines), for perovskite colloids prepared with C4, $MAPbI_x$ perovskite precursors and cOEA ligands. cOEA was added to an <*n*> = 2 precursor mixture of $C4_2MAPb_2I_7$ prior to antisolvent precipitation for an effective stoichiometry of $cOEA_{2x}\{C4_2MAPb_2I_7\}$. Transmission WAXS (a) was measured for ~ 10 mmol Pb/L dispersions in toluene, whereas optical transmittance (b) was measured for ~ 0.1 mmol Pb/L dispersions in toluene. Grazing-incidence WAXS, at an incidence angle of 0.1 degrees, was measured for drop-cast films in (a), and normal-incidence transmittance was measured for drop-cast films in (b), of approximately the same thickness. All WAXS and transmittance data were normalized by intensity.

Substituted C12 or cOEA ligands for <*n*> = 2 $C4_2MAPb_2I_7$

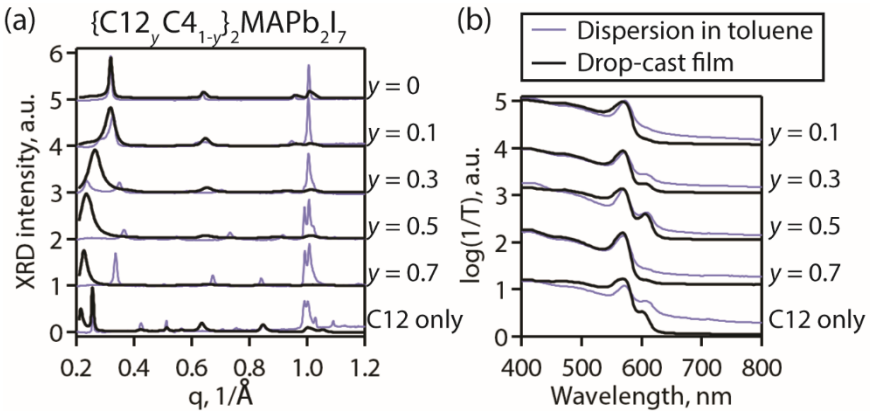

Figure S15. a) Wide-angle X-ray scattering (WAXS) and b) transmittance measurements of either colloidal dispersions in toluene (light blue lines) or drop-cast films of the same dispersions on quartz (black lines), for perovskite colloids prepared with C4, $MAPbI_x$ perovskite precursors and C12 ligands. C12 was substituted for C4 in <*n*> = 2 precursor solutions prior to antisolvent precipitation for an effective stoichiometry of $\{C12_yBA_{1-y}\}_2MAPb_2I_7$. Transmission WAXS (a) was measured for ~ 10 mmol Pb/L dispersions in toluene, whereas optical transmittance (b) was measured for ~ 0.1 mmol Pb/L dispersions in toluene. Grazing-incidence WAXS, at an incidence angle of 0.1 degrees, was measured for drop-cast films in (a), and normal-incidence transmittance was measured for drop-cast films in (b), of approximately the same thickness. All WAXS and transmittance data were normalized by intensity.

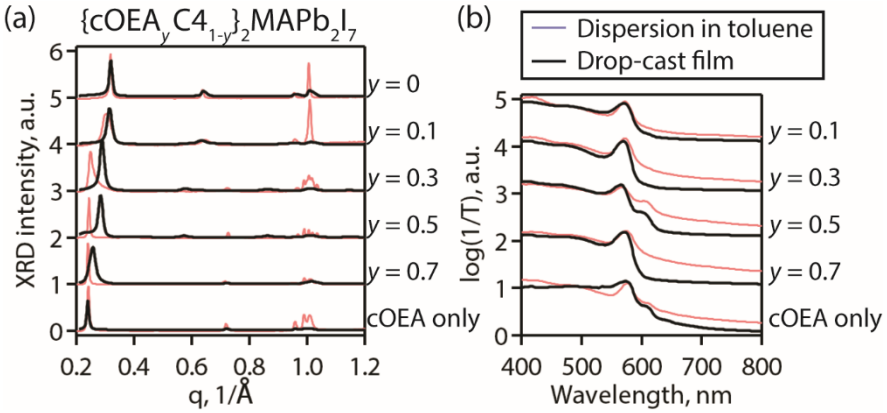

Figure S16. a) Wide-angle X-ray scattering (WAXS) and b) transmittance measurements of either colloidal dispersions in toluene (light red lines) or drop-cast films of the same dispersions on quartz (black lines), for perovskite colloids prepared with C4, $MAPbI_x$ perovskite precursors and cOEA ligands. cOEA was substituted for C4 in <*n*> = 2 precursor solutions prior to antisolvent precipitation for an effective stoichiometry of $\{cOEA_yBA_{1-y}\}_2MAPb_2I_7$. Transmission WAXS (a) was measured for ~ 10 mmol Pb/L dispersions in toluene, whereas optical transmittance (b) was measured for ~ 0.1 mmol Pb/L dispersions in toluene. Grazing-incidence WAXS, at an incidence angle of 0.1 degrees, was measured for drop-cast films in (a), and normal-incidence transmittance was measured for drop-cast films in (b), of approximately the same thickness. All WAXS and transmittance data were normalized by intensity.

Small angle neutron scattering (SANS) measurements and models

All fits to the SANS measurements and scattering simulations were completed using SASView software. The fits to the three power law, cylinder, and parallelepiped models were completed using Levenberg-Marquardt curve fitting while the stacked disk model was fit using the DREAM algorithm. Prior to fitting, the incoherent background scattering was subtracted from the intensity. The incoherent background scattering was found by fitting a line to a plot of q^4 *vs* Iq^4. The slope of this line provides the background intensity for sufficiently high q.

Three power law model. The empirical three power law model captures the main features of the measured SANS from the colloidal dispersions discussed in this work. The model does not prescribe a physical structure, but rather enables the extraction of the scaling of scattered intensity with q (*i.e.* $I(q) \sim Aq^{-m}$, where A is a constant prefactor, q is the wavevector and m is the power law exponent). The extracted scaling exponents and crossovers between the various scaling regimes can then be linked to features of the structure. The three power law model was employed to capture the three observed regimes of the coherent scattering intensity with varying q. In this model, the coherent scattering intensity is

$$I(q) = \begin{cases} Aq^{-m_1}; q \leq q_{c,1} \\ Bq^{-m_2};\ q > q_{c,1}\ and\ q \leq q_{c,2} \\ Cq^{-m_3}; q > q_{c,2} \end{cases}$$

Where m_1, m_2 and m_3 are the power law scaling exponents; $q_{c,1}$ and $q_{c,2}$ are the crossovers from region 1 to region 2 and region 2 to region 3 respectively; and A, B and C are scaling exponents that are specified to produce similar intensities at the crossover points between neighboring regions. In this work, we are concerned with the power law exponents in the high, mid, and low q as well as the crossover between these regions.

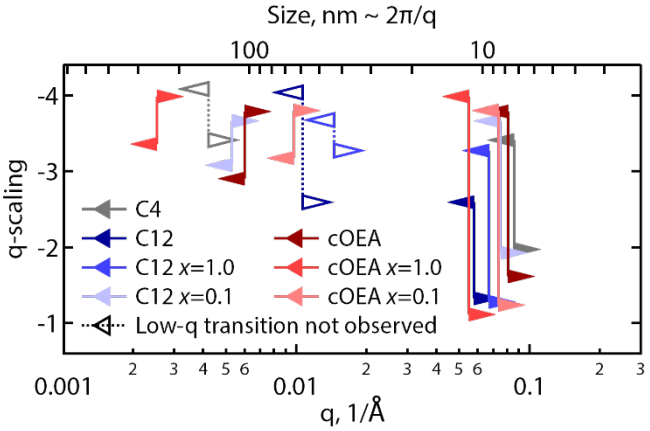

Figure S17. Estimated parameters for the three power law fits of the SANS data shown in **Figure 7a**. The markers indicate the transition in q-scaling between different regimes of the data. The direction of the arrow indicates whether the q-scaling value corresponds to larger or smaller q values. The open markers with dashed lines indicate that no transition was observed at low q from $\sim q^{-4}$ to $\sim q^{-3}$. For these samples, the 'size' of R-P particles was estimated from the lowest q-value measured (**Figure 7b,c**).

Table S2. Fitting parameters extracted from three power law fits of SANS patterns shown in **Figure 7a**.

Sample	Low q scaling	Low-to-mid crossover q, 1/Å	Mid q scaling	Mid-to-high crossover q, 1/Å	High q scaling	Background, cm^{-1}
cOEA **only**	2.9004 ± 0.012235	0.0060117 ± 5.989E-5	3.7861 ± 0.0040401	0.081105 ± 0.0021186	1.6153 ± 0.065035	0.026747
cOEA ***x* = 1.0**	3.3558 ± 0.052433	0.0025339 ± 9.1427E-5	3.987 ± 0.0044556	0.05514 ± 0.0028244	1.1127 ± 0.049103	0.034677
cOEA ***x* = 0.1**	3.1717 ± 0.007281	0.0097727 ± 9.1444E-5	3.802 ± 0.0065835	0.07367 ± 0.0017843	1.2421 ± 0.028083	0.032850
C12 **only**	4.0351 ± 0.030691	0.010678 ± 0.0002138	2.5916 ± 0.045054	0.057786 ± 0.0072418	1.3244 ± 0.0797	0.012791
C12 ***x* = 1.0**	3.6756 ± 0.0071928	0.014536 ± 0.00044472	3.27 ± 0.021865	0.067198 ± 0.0020501	1.2765 ± 0.037078	0.020502
C12 ***x* = 0.1**	3.0807 ± 0.015795	0.0053205 ± 0.00010055	3.6604 ± 0.0041533	0.075242 ± 0.0016977	1.9288 ± 0.064701	0.017943
C4 **only**	4.0843 ± 0.23126	0.0042068 ± 0.0001024	3.4079 ± 0.0036863	0.085774 ± 0.0032381	1.9718 ± 0.073458	0.018886

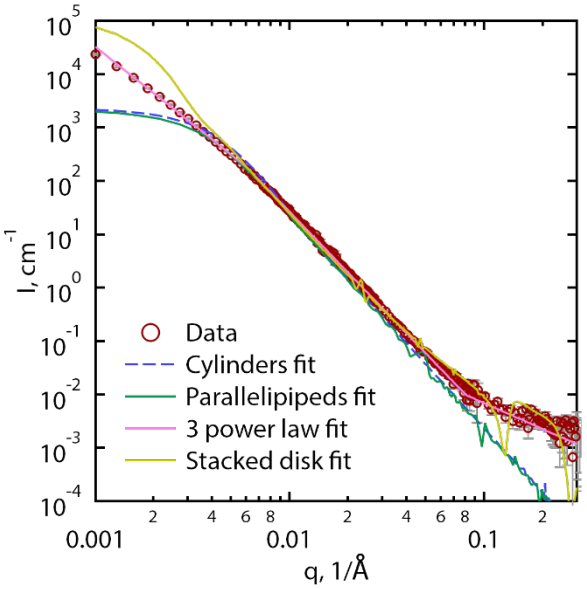

Figure S18. A comparison of different models used to fit SANS data for <*n*> = 2 colloids prepared with only cOEA spacers, as shown in **Figure 7a**. The dark red circles are measured data points, the dashed blue line is a fit to a model of cylinders, the solid light green line is a fit to a model of parallelepipeds, the solid pink line is the 3 power law fit shown in **Figure 7a**, and the solid light orange line is a fit to a model of stacked disks.

Cylinder and parallelepiped models. Polydisperse cylinder and parallelepiped models were employed to determine if a simpler description of the structure could describe the measured scattering. The coherent scattering intensity for the cylinder model is calculated as[5]

$$I(q) = Scale \int_0^{\pi/2} \pi R^2 L \left(\frac{\sin\left(\frac{1}{2} qL\cos(\alpha)\right)}{\frac{1}{2} qL\cos(\alpha)} \frac{J_1(qR\sin(\alpha))}{qR\sin(\alpha)} \right)^2 \sin(\alpha)\, d\alpha$$

where *Scale* is a constant factor of proportionality, R is the cylinder radius, L is the cylinder length, and J_1 is the first order Bessel function. The coherent scattering intensity for the parallelepiped model is calculated as[6]

$$I(q) = Scale \int_0^1 ABC\ \phi_Q\left(\mu\sqrt{1-\sigma^2}, \frac{A}{B}\right) S\left(\frac{qC\sigma}{2}\right) d\sigma$$

$$\phi_Q(\mu, a) = \int_0^1 \left\{ S\left[\frac{qB}{2}\cos\left(\frac{\pi}{2}u\right)\right] S\left[\frac{qa}{2}\sin\left(\frac{\pi}{2}u\right)\right] \right\}^2 du$$

$$S(x) = \frac{\sin(x)}{x}$$

where *Scale* is a constant factor of proportionality; A, B and C are the sides of the parallelepiped (with $A<B<C$).

A Gaussian polydispersity in the dimensions of the particles was applied for these models. For the cylinder model, the standard deviation of radii was fixed at $0.5\langle R\rangle$ and the standard deviation of the length was fixed at $0.1\langle R\rangle$. For the parallelepiped model, the standard deviations for the two shorter lengths were fixed at $0.5\langle A\rangle$ and $0.5\langle B\rangle$ while the longer length was fixed at $0.1\langle C\rangle$ These standard deviations were chosen because they were found to be sufficient to dampen oscillations in the scattering intensity coming from reflections from monodisperse particles. The longest dimension of the particles (L for the cylinder and C for the parallelepiped) was fixed to $D_{scherrer}$ measured from SAXS.

For the included fit to the cylinder model for the "COEA only" sample, the cylinder fit converged at $\langle R\rangle$ = 247.99 ± 0.4195 Å while the parallelepiped fit converged at $\langle A\rangle$ = 389.11 ± 0.44937 Å and $\langle B\rangle$ = 775.58 ± 1.1609 Å. However, these simple models do not fit the SANS data across the entire range of q-values, and diverge at low and high q-values (**Figure S18**).

Stacked disk model. The scattering length densities of the perovskite, spacer, and solvent were fixed based upon an estimate for the atomic composition and density of the layers and solvent (**Table S4**). The perovskite and spacer layer sizes were taken from the most populous d-spacing and n-value from the transmission WAXS measurements for each individual sample (**Table S1**). The number of layers and standard deviation in number of layers were also taken from the $D_{scherrer}$ measured with WAXS. Fixing the aforementioned parameters leaves four parameters to fit: the volume fraction of platelet stacks, the incoherent background scattering, the standard deviation in d-spacing, and the radius (*i.e.* 0.5× grain 'width' defined in **Figure 2**) of the stacked disks. The volume fraction and incoherent background are independent of the finer features of the structure, so only two adjustable parameters are fit to the structure. Due to oscillations in the scattering predictions from monodisperse radii of platelets, a Gaussian distribution of radii was implemented where the standard deviation of radii was fixed at $0.5\langle R\rangle$ where $\langle R\rangle$ is the average radius of the disks. This standard deviation was chosen because it was found to dampen oscillations in the scattering intensity coming from reflections from monodisperse platelets.

The stacked disk model[7] is given as

$$I(q) = Scale \int_0^{\pi/2} \left[\Delta\rho_t\left(V_s f_s(q,\alpha) - V_c f_c(q,\alpha)\right) + \Delta\rho_c V_c f_c(q,\alpha)\right]^2 S(q,\alpha)\sin(\alpha)\, d\alpha + bkgd$$

$$f_s(q,\alpha) = \left(\frac{\sin(q(d+h)\cos(\alpha))}{q(d+h)\cos(\alpha)}\right)\left(\frac{2J_1(qR\sin(\alpha))}{qR\sin(\alpha)}\right)$$

$$f_c(q,\alpha) = \left(\frac{\sin(qh\cos(\alpha))}{qh\cos(\alpha)}\right)\left(\frac{2J_1(qR\sin(\alpha))}{qR\sin(\alpha)}\right)$$

$$S(q) = 1 + \frac{1}{2}\sum_{k=1}^{n}(n-k)\cos(2k(d+h)q\cos(\alpha))\exp\left(-\frac{kq^2(2(d+h)\cos(\alpha\sigma_d))^2}{2}\right)$$

where $\Delta\rho_i$ is the scattering length density difference between the perovskite core ($i = c$) or spacer ($i = s$) and the solvent; V_i is the volume of the perovskite core ($i = c$) or spacer ($i = s$); h is the thickness of the core layer; d is the thickness of the spacer layer; R is the radius of the disks; n is the number of stacked disks; and σ_d is the standard deviation of the d-spacing. The stacked disk model assumes uniform scattering length density in equal radii layers. The number of stacked disks was calculated from the measured $D_{scherrer}$, thickness of spacer layer, and thickness of core as $n = \frac{D_{scherrer}}{d+h}$ from XRD. The spacer thickness was taken as the interlayer d-spacing and the core thickness was calculated based upon the n-value as $h = n(6.4\ \text{Å})$. The variation in d-spacing is assumed to be Gaussian; the polydispersity in number of stacks is Gaussian with a standard deviation set by the measured standard deviation in $D_{scherrer}$, and the standard deviation in the disk radius is assumed to be Gaussian with a standard deviation of $0.5\langle R\rangle$ where $\langle R\rangle$ is the average disk radius. Scattering length densities (SLDs) were estimated based on atomic densities of approximate compositions of each layer in the stacked disk model described above (**Table S4**). Densities of the lead iodide octahedral layers and the interlayer spacers were estimated from by the approximations described previously (**Figure S1**). However, the SANS fits used an approximate average of estimated SLDs between the different n-values and spacer compositions to simplify the model. The average SLD of the perovskite, spacer, and solvent were taken as 1.0×10^{-6}, -0.5×10^{-6}, and 5.7×10^{-6} Å^{-2} respectively. These values of the scattering length density assume that no solvent enters into the perovskite or spacer layers.

Table S3. Scattering length densities and coherent scattering cross sections calculated for the solvent and layers for a stacked disk model of SANS scattering.

Layer	Composition	Density, g/cm^3	SLD, 10^{-6}/Å^2
Toluene	C_7D_8	0.943	**5.664**
n = 1 PbI_x layer	PbI_4	4.8	1.234
n = 2 $MAPbI_x$ layer	$CNH_6Pb_2I_7$	4.4	0.979
n = 3 $MAPbI_x$ layer	$C_2N_2H_{12}Pb_3I_{10}$	4.3	0.903
n = 3 $MAPbI_x$ layer	$C_3N_3H_{18}Pb_4I_{13}$	4.2	0.854
C12	$C_{12}NH_{28}$	0.95	-0.479
cOEA	$C_{10}NH_{22}$	1.1	-0.274
C4	C_4NH_{12}	0.9	-0.653
Avg. Lead iodide layer	N/A	N/A	**1.0**
Avg. Interlayer spacers	N/A	N/A	**-0.5**

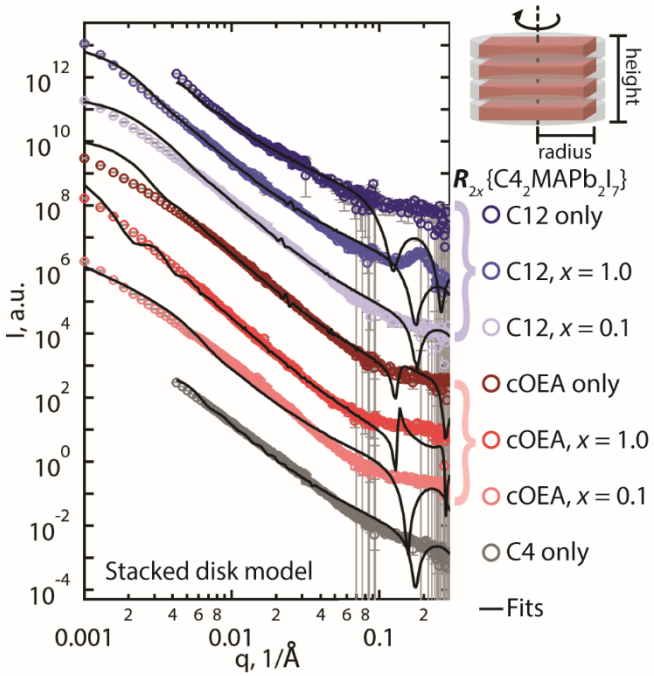

Figure S19. Transmission small angle neutron scattering (SANS) patterns from ~10 mmol Pb/L colloidal dispersions in deuterated toluene prepared with C4 spacers, $MAPbI_x$ perovskite precursors and added C12 or cOEA. Patterns were offset by a constant multiplicative factor for easier comparison of the data. Fits of SANS data to a stacked disk model of R-P phases, as illustrated in the upper right, are shown as solid black lines.

Table S4. Parameters extracted from fits of SANS patterns to the stacked disk model for the data and fits shown in **Figure S19**.

Sample, $\{R_2\}_x\{C4_2MAPb_2I_7\}$	Particle radius, Å	Interlayer *d* standard deviation, Å	Scale	Background, cm^{-1}
cOEA **only**	7675.2 ± 41.167	0.37219 ± 0.0011075	0.0019323 ± 6.5304E-6	0.026747
cOEA ***x* = 1.0**	779.9 ± 0.45973	0.42102 ± 0.002463	0.00099588 ± 4.1977E-6	0.034677
cOEA ***x* = 0.1**	1191.2 ± 1.2987	0.58152 ± 0.002413	7.8994E-5 ± 5.7165E-6	0.032850
C12 **only**	1150.2 ± 1.6451	0.29297 ± 0.001343	0.0025992 ± 8.2739E-6	0.012791
C12 ***x* = 1.0**	844.17 ± 0.18561	0.16151 ± 0.001191	0.00383 ± 9.0496E-6	0.020502
C12 ***x* = 0.1**	5028.1 ± 38.718	0.078974 ± 0.0008798	0.0057003 ± 4.6585E-6	0.017943
C4 **only**	906.53 ± 0.4359	0.27438 ± 0.0015348	0.0025066 ± 6.6543E-6	0.018886

SANS simulations of nanoplatelets.

Figure S20d shows SANS simulations based on a model of stacked disks for dispersed single-sheet nanoplatelets with 5 nm radii. Modeled nanoplatelets with n = 1-4 all show a transition around $q \sim 0.05$ 1/Å (10 nm in real space) from $\sim q^{-4}$ scaling at high q to flat q^0 response at low q. The n-value has a negligible impact on the simulated SANS pattern (**Figure S20d**). The simulated SANS spectra of exfoliated nanoplatelets is substantially different from simulated SANS spectra of larger stacked disks (**Figure S20b,c**) and experimental SANS spectra (**Figure 7**). Diluting the perovskite dispersion, even up to 100×, has a negligible impact on the SANS spectra (**Figure S21**). Thus, the colloidal perovskites are mostly large ($\gg$ 10 nm) crystallites.

If the colloidal dispersion contained distinct populations of large crystallites and small, exfoliated nanoplatelets, then the nanoplatelets would cause a distinct scattering signal in the mid-q range of the SANS spectra. SANS is quantitatively sensitive to the number of scattering nuclei in the beam path, and can, in principle, be used to estimate the ratios of different colloid morphologies in a polydisperse sample. The experimental data lacks sufficient texture to use quantitative fits to answer this question, but simulations can be used to place a rough bound on the presence of exfoliated nanoplatelets. **Figure S20e** shows linear convolutions of nanoplatelet (1 layer thick, n = 2, 5 nm radius, **Figure S20d**) and stacked-disk crystallite (100 layers, n = 2, 50 nm radius, **Figure S20c**) simulations. The convolutions were scaled by the number of nuclei in each structure because large R-P crystallites have much larger volume per particle than exfoliated nanoplatelets. The dispersion is assumed to be dilute enough that the two populations scatter independently.

The convolutions shown in **Figure S20e** reveal that a large population of exfoliated nanoplatelets (> 10%, measured by the number fraction of nuclei in nanoplatelets) would yield shallow q-scaling in the range of 0.01 Å < q < 0.1 Å, followed by steeper q-scaling at q < 0.01 Å. However, experimental SANS spectra show consistently steep q scaling in this region for all samples (except perhaps for the C12-only sample in **Figure 7**). Without sharper features in the SANS spectra it is difficult to make more quantitative estimates of the colloidal morphology. Nonetheless, these simulations indicate that exfoliated nanoplatelets are a minority structure (< 10 % nuclei number ratio) in these dispersions, rather than a significant unresolvable population.

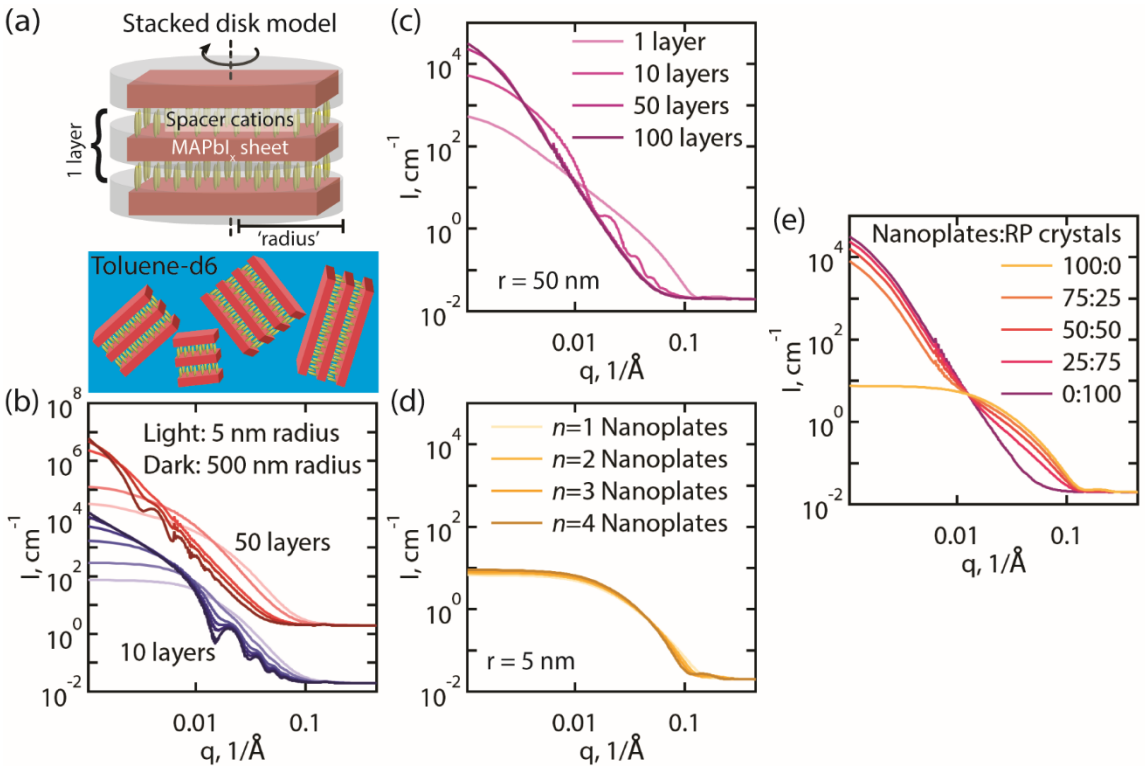

Figure S20. Simulated transmission small angle neutron scattering (SANS) patterns for a stacked-disk model of dispersed colloids, as described in the section above ('**Stacked disk model**'). a) The stacked disk model is defined by the scattering cross-sections and thickness of alternating layers (*i.e.* the insulating spacer layer and inorganic perovskite layer), as well as the number of stacked layers, radius of the stacked disk, and polydispersity in each of these parameters. The model assumes a randomly-oriented ensemble of stacked disks within a deuterated toluene solvent. b) SANS simulations comparing the effect of the grain radius, ranging from 5 nm to 500 nm, for 10 layer and 50 layer stacked disks ($n = 2$). c) SANS simulations comparing the effect of the number of layers of stacked disks for 50 nm radius grains ($n = 2$). d) SANS simulations of single-layer disks with 5 nm radius for perovskite sheet layers reflecting n = 1-4 R-P phases. e) A convolution of simulations of 50 nm radius, 50 layer stacked disks from (c) with 5 nm radius, single-layer disks ($n = 2$) from (d). The ratios shown in (e) indicate the number ratio of nuclei present in each phase, and assumes that the two populations are sufficiently dilute that they scatter independently. For all simulations, the standard deviation in the disk radius is assumed to be Gaussian with a standard deviation of $0.5\langle R\rangle$, where $\langle R\rangle$ is the average disk radius.

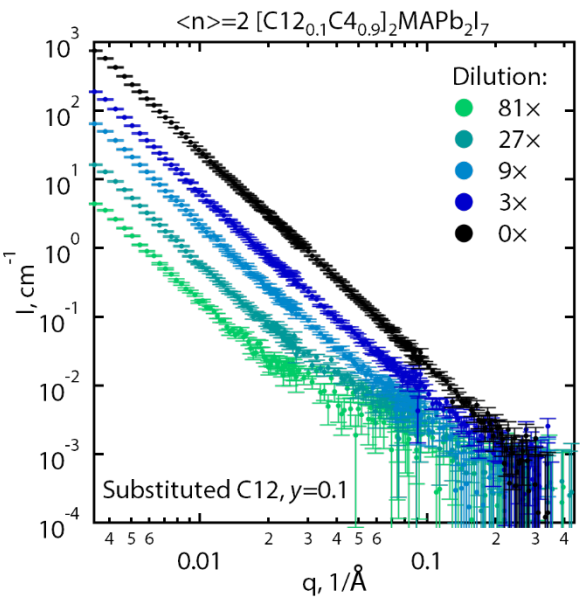

Figure S21. A comparison of transmission small angle neutron scattering (SANS) patterns for dilutions of a colloidal dispersion prepared with a precursor stoichiometry of $(C12_{0.1}C4_{0.9})_2MAPb_2I_7$, corresponding to the y = 0.1 'substitutional' stoichiometry with C12 spacers shown in **Figures S10** and **S11**. The same low q scaling is observed regardless of dilution, ranging from ~ 10 mmol Pb/L (0× dilution) to ~ 0.1 mmol Pb/L (81× dilution). The difference in scaling at high q is due to background incoherent scattering, and thus low signal-to-noise, at lower intensities.

References

(1) Stoumpos, C. C.; Cao, D. H.; Clark, D. J.; Young, J.; Rondinelli, J. M.; Jang, J. I.; Hupp, J. T.; Kanatzidis, M. G. Ruddlesden–Popper Hybrid Lead Iodide Perovskite 2D Homologous Semiconductors. *Chem. Mater.* **2016**, *28*, 2852–2867.

(2) Billing, D. G.; Lemmerer, A. Synthesis, Characterization and Phase Transitions of the Inorganic–Organic Layered Perovskite-Type Hybrids $[(C_nH_{2n+1}NH_3)_2PbI_4]$ (n = 12, 14, 16 and 18). *New J. Chem.* **2008**, *32*, 1736–1746.

(3) Stoumpos, C. C.; Malliakas, C. D.; Kanatzidis, M. G. Semiconducting Tin and Lead Iodide Perovskites with Organic Cations: Phase Transitions, High Mobilities, and Near-Infrared Photoluminescent Properties. *Inorg. Chem.* **2013**, *52*, 9019–9038.

(4) Sichert, J. A.; Hemmerling, A.; Cardenas-Daw, C.; Urban, A. S.; Feldmann, J. Tuning the Optical Bandgap in Layered Hybrid Perovskites through Variation of Alkyl Chain Length. *APL Materials* **2019**, *7*, 041116.

(5) Guinier, A.; Fournet, Gerard. *Small-Angle Scattering of X-Rays*; Structure of Matter Series; John Wiley & Sons, Inc.: New York, NY, 1955.

(6) Mittelbach, P; Porod, G. X-Ray Low-Angle Scattering by Dilute Scattering Colloidal Systems. The Calculation of Scattering Curves of Parallelepipeds. *Acta Phys. Austriaca* **1961**, *14*, 185–211.

(7) Kratky, O.; Porod, G. Diffuse Small-Angle Scattering of X-Rays in Colloid Systems. *J. Colloid Sci.* **1949**, *4*, 35–70.